Partitioning of Ru, Rh, Pd, Re, Ir, and Au between Cr-bearing spinel, olivine, pyroxene and silicate melts.

K. Righter†, Lunar and Planetary Laboratory, University of Arizona, Tucson, AZ 85721

A. J. Campbell and M. Humayun, Dept. of the Geophysical Sciences, 5734 S. Ellis Ave., University of Chicago, Chicago, IL 60637

R. L. Hervig, Center for Solid State Science, Arizona State University, Tempe, AZ 85287

† now at: Mailcode ST, NASA Johnson Space Center, 2101 NASA Rd. 1, Houston, TX 77058.

Abstract

A series of high temperature experiments was undertaken to study partitioning of several highly siderophile elements (HSE; Ru, Rh, Pd, Re, Os, Ir, Pt and Au) between Cr-rich spinel, olivine, pyroxene and silicate melt. Runs were carried out on a Hawaiian ankaramite, a synthetic eucrite basalt, and a DiAn eutectic melt, at one bar, 19 kbar, and 20 kbar, respectively, in the temperature range of 1200 to 1300 ˚C, at oxygen fugacities between the nickel-nickel oxide (NNO) and hematite-magnetite (HM) oxygen buffers. High oxygen fugacities were used to suppress the formation of HSE-rich "nuggets" in the silicate melts. The resulting oxide and silicate crystals (<100 μm) were analyzed using both SIMS and LA-ICP-MS, with a spatial resolution of 15 to 50 microns. Rhenium, Au and Pd were all found to be incompatible in Cr-rich spinel ($D_{\mathrm{Re}}^{sp/melt} = 0.0012 - 0.21, D_{Au}^{sp/melt} = 0.076, D_{Pd}^{sp/melt} = 0.14$), whereas Rh, Ru and Ir were all found to be highly compatible ($D_{Rh}^{sp/melt} = 41 - 530, D_{Ru}^{sp/melt} = 76 - 1143, D_{Ir}^{sp/melt} = 5 - 22000$). Rhenium, Pd, Au and Ru were all found to be incompatible in olivine ($D_{\mathrm{Re}}^{oliv/melt} = 0.017 - 0.073, D_{Pd}^{oliv/melt} = 0.12, D_{Au}^{oliv/melt} = 0.12, D_{Ru}^{oliv/melt} = 0.23$), Re is incompatible in orthopyroxene and clinopyroxene ($D_{\mathrm{Re}}^{opx/melt} = 0.013, D_{\mathrm{Re}}^{cpx/melt} = 0.18 - 0.21$), and Pt is compatible in clinopyroxene ($D_{Pt}^{cpx/melt} = 1.5$). The results are compared to and combined with previous work on HSE partitioning among spinel-structured oxides, and applied to some natural magmatic suites to demonstrate consistency.

Introduction

Spinels are a common liquidus phase in ultrabasic and basic melts and are known to control transition metal concentrations (e.g., Ni, Co, Cr, V) in magmas during differentiation (e.g., Irving, 1978). Many magmatic suites show correlations between Ni or Cr with highly siderophile elements (HSEs, which are the platinum group elements, Au and Re), especially Ir, Ru and Os (e.g., Brügmann et al., 1987; Puchtel and Humayun, 2000; Righter et al., 2000; Puchtel and Humayun, 2001). Oxide mineral separates from ore deposits are commonly enriched in HSE (Agiorgitis and Wolf, 1978; Auge, 1988; Page, 1984; Parry, 1984; Razin and Khomenko, 1969). Furthermore, many experimental studies (Capobianco, 1993, 1998; Krutsch and Kemmler-Sack, 1983; Righter and Downs, 2001) have produced HSE-rich oxides, showing the potential importance of these phases in hosting such elements. Whether the correlations between Ni and HSEs are due to olivine or chromian-spinel fractionation (or both), or require the fractionation of trace HSE minerals, has remained uncertain, but resolution of this question is important for a better understanding of HSE behavior in basic and ultrabasic systems (e.g., Puchtel and Humayun, 2001).

Experimental efforts to resolve this problem have so far focused on Fe^{3+}- and Al-bearing spinels (Capobianco and Drake, 1990; Capobianco et al., 1994). These studies have demonstrated a clear compatibility of Ru and Rh in such spinels, as well as incompatibility of Pd. However, applicability of these results to basaltic and ultrabasic systems may be inappropriate due to large differences in crystal chemistry and issues of inverse (e.g., magnetite) vs. normal (e.g., spinel or chromite) spinels.

An additional hindrance to progress on spinels is the so-called nugget effect that plagues ex-

perimental geochemistry of the HSEs. The solubility of HSEs (e.g., Pt, Rh and Pd) in silicate melts exhibits apparently anomalous behavior at oxygen fugacities of QFM and below (e.g., Ertel et al., 1999; Borisov and Palme, 1996); solubilities are no longer a clear function of oxygen fugacity at these conditions, but rather show a generally flat slope with considerable scatter in the experimental data. It is thought that this anomalous behavior is due to the presence of nanometer scale metallic flakes that are suspended within the silicate melt, interfering with the analysis and thus obscuring the true solubility of the element in silicate melt (e.g., Lindstrom and Jones, 1996). As this problem is not well understood or constrained, it has been necessary to carry out experiments at high oxygen fugacity, where the above effects are not observed. Although this high fO_2 region does not overlap with the range of oxygen fugacities defined by MORB or abyssal peridotite, it is within the field of more oxidized terrestrial magmas. An understanding of HSE partitioning at high fO_2 conditions can be extrapolated to aid our interpretation of low fO_2 magmas.

A final obstacle for previous HSE partitioning experimentation has been the choice of analytical technique. Crystals grown in experimental systems are small (25 to 100 μm), and preclude mineral separations or preconcentrations for bulk analyses. Therefore, the small mineral grains must be analyzed by a microanalytical technique with comparable spatial resolution. Electron microprobe analysis (EMPA), of course, offers the necessary resolution, but solubilities of HSE in silicate melts are all below detection limits for EMPA. Secondary ion mass spectrometry (SIMS) offers good spatial resolution (~15 micron spot), but only a few of the HSE (e.g., Rh, Re) are ionized well enough to allow analysis. Laser ablation ICP-MS (LA-ICP-MS) allows analysis of all the HSE at very high sensitivity, but because sensitivity is a function of laser spot size, analysis of small experimental samples can be compromised.

In a new set of experiments, we widen the compositional range of experimentally determined spinel-melt partitioning to include Cr-rich spinels. Several runs also contained olivine or pyroxene, and partition coefficients for these phases were measured as well. Runs were carried out at oxygen fugacities between the nickel-nickel oxide (NNO) and hematite-magnetite (HM) oxygen buffers, and are analyzed using both SIMS and LA-ICP-MS. The results are compared to previous work on HSE partitioning among spinel-structured oxides. The new experimental partition coefficients are also compared with partitioning observed in natural mineral-melt pairs (Puchtel and Humayun, 2001) and then applied to explain the HSE fractionation trends in natural magmatic suites from Kostomuksha (Puchtel and Humayun, 2000), Vetreny (Puchtel and Humayun, 2001), Cape Smith Fold Belt (basaltic komatiites; Barnes and Picard, 1993) and Hawaii (HSDP basalt; Hauri et al., 1996; Rhodes, 1996), for which published HSE data are available.

Experimental

Three different compositions were selected for this study (Table 1). First, a Hawaiian ankaramite was selected because it has spinel and olivine stable across a large fO_2 range, and thus is applicable to many basaltic systems. The iron-free diopside-anorthite system eutectic composition was used to study clinopyroxene-melt partitioning, so that unusual Fe^{3+}-bearing clinopyroxenes would not be stable at high fO_2. Glass of this composition was prepared by multiple rounds of fusion and grinding of high purity CaO, MgO, SiO_2 and Al_2O_3 in a Pt crucible, in air. Finally, a synthetic eucrite basalt composition was selected in order to study pyroxene-melt partitioning, since the eucritic basalt composition has orthopyroxene stable as a liquidus phase (e.g., Schwandt and McKay, 1998; Stolper, 1977). Powder of this composition was prepared by grinding and sintering of high purity Fe_2O_3, CaO, MgO, SiO_2 and Al_2O_3 in a Pt crucible, in air.

Each ankaramite experiment was doped to the 1 wt% level with 3 of the following elements: Cr, Ni, Ru, Rh, Re, Os, Ir (Table 2). These compositions were placed in 3 mm AuPd capsules and crimped at the top. These capsules were then sealed, together with a buffer mixture in an alumina crucible, into an evacuated silica tube. Buffers used were hematite-magnetite (HM), MnO-Mn_3O_4 (MHO), Re-ReO_2 (RRO), and Ni-NiO (NNO), covering ~5.5 log fO_2 units at 1300 ˚C (Fig. 1). The silica tubes were held in the hotspot of vertical 1 atm furnaces for 48 hr and then quenched by rapid removal from the furnace. All runs contained spinel and glass (Fig. 2), most contained metal (identified by energy dispersive spectrometry or electron microprobe analysis) and several contained olivine (Table 2).

For the experiment using the DiAn eutectic composition, the starting material was equilibrated with Re and Pt metal, in an evacuated silica tube buffered at the HM buffer at 1300 ˚C. This run was specifically designed to measure the partitioning of Pt and Re between clinopyroxene and silicate melt at high oxygen fugacities. Large clinopyroxenes grown during this experiment were conducive to LA-ICP-MS analysis.

Two experiments at higher pressures were also included in this study. Runs 112 and 118 were carried out in a piston cylinder apparatus, at 19 and 20 kb, respectively, and a temperature of 1275 ˚C. Both Re-doped synthetic eucrite basalt and Ru-RuO_2 oxygen buffer materials were encapsulated by Pt, which was welded shut using an argon plasma welder. Run 112 produced Ni-bearing spinel, two pyroxenes, Ru metal and silicate melt (Fig. 2). Run 118 produced Ni-bearing spinel, Ru metal, RuO_2 and glass. The oxygen fugacity of Run 118 was buffered by the Ru-RuO_2 oxygen buffer, and calculated (Table 2) at P and T using data reported and cited by O'Neill and Nell (1997); the oxygen fugacity of Run 112 was only constrained to be below the

Ru-RuO_2 oxygen buffer, since RuO_2 was not present. The concentration of Re in the silicate melt (156 ppm) suggests that the oxygen fugacity was perhaps several log fO_2 units below the Ru-RuO_2 buffer. The oxygen fugacity differences between Runs 112 and 118 can account for the distinct mineralogy of these two runs, despite similar P and T conditions.

Analytical

Electron microprobe

A CAMECA SX50 electron microprobe was used to analyze major elements, Ni, Co and Cr in experimental glasses, spinels, olivines and metals (Tables 3 through 6). Operating conditions were an accelerating voltage of 15 kV and beam currents of 10 nA. Standards include both natural (albite, diopside, potassium feldspar, fayalite, rhodonite, apatite, chromite) and synthetic (Ni, Co, HSE metals, TiO_2) materials. PAP □□□□□ corrections were used in the data reduction (Pouchou and Pichoir, 1991). FeO and Fe_2O_3 in spinels were calculated by charge balance and stoichiometry. Most spinels produced in the new experiments reported here contain a large amount of Cr (Table 3), but there is a range of compositions produced by variable oxygen fugacity.

Secondary ion mass spectrometry (SIMS)

Ruthenium, Rh and some Ni contents of glasses were analyzed using secondary ion mass spectrometry (SIMS) with a CAMECA 6f ion probe at ASU (Table 7). SIMS analyses were obtained with a 1 nA primary beam of $^{16}O_2^-$ ions focused to a 10-15 □m spot. Positive secondary ions with excess kinetic energies of 75 ± 20 eV were allowed into the mass spectrometer. Each analysis consisted of a 5 minute pre-sputter period followed by collection of secondary ion

intensities for ^{30}Si, ^{101}Ru, ^{103}Rh, and ^{60}Ni for time sufficient to reach integrated signals of at least 100 counts and usually 500 counts. Ruthenium- and Rh-bearing basaltic glasses (from Capobianco et al., 1994) were used as standards from which calibration curves of $^{101}Ru^{+}/^{30}Si^{+}$ vs. Ru (ppm) and $^{103}Rh^{+}/^{30}Si^{+}$ vs. Rh (ppm) were constructed (Fig. 3). Several runs contained small concentrations of Ni (< 300 ppm) and these were also determined by SIMS using a set of Ni-bearing glasses as standards (from Righter, 2002). Typical error on a SIMS trace element analysis is 10% (20% error on a given partition coefficient; Table 7), and is attributable mainly to counting statistics.

Laser ablation ICP-MS

Trace element concentrations of several HSEs were analyzed by laser ablation ICP-MS (Table 8). Locations to be analyzed were first selected from polished sections of the experimental run products, using backscattered electron images acquired with either the SX-50 electron microprobe (Arizona) or the JEOL 5800-LV scanning electron microscope (SEM) at The University of Chicago. Laser ablation ICP-MS analyses were performed using a CETAC LSX-200 laser ablation peripheral with a magnetic sector ICP mass spectrometer, the Finnigan Element™, using techniques similar to those described in Campbell and Humayun (1999) and Campbell et al. (2002). The dimensions of each laser ablation pit were adjusted according to the grain size of the phase being analyzed, and ranged from 15 to 100 μm in diameter and approximately 10 to 25 μm deep. The laser was operated at 10 Hz for 2 to 5 seconds for each analysis, and data collection from the mass spectrometer continued for ~20 sec as the signal reached a maximum and decayed away. During data collection the mass spectrometer was swept repeatedly over the mass range of interest with a period of about 0.7 sec, and counts were accumulated at selected masses. A subset

of the following isotopes was monitored during each analysis: ^{25}Mg, ^{53}Cr, ^{57}Fe, ^{60}Ni, ^{101}Ru, ^{103}Rh, ^{105}Pd, ^{187}Re, ^{192}Os, ^{193}Ir, ^{195}Pt, ^{197}Au. These isotopes were chosen to maximize signal-to-noise ratios and to minimize overlap with isotopes of neighboring elements or background sources, particularly $^{12}C^{12}C^{+}$, $^{40}Ar^{14}N^{+}$, and $^{40}Ar^{16}O^{+}$. Background and isobaric interferences were subtracted from the time-integrated signal using the average of 3 blank measurements that were run immediately before and/or after each set of analyses; the detection limit of each measurement was set as 3 standard deviations above the average blank.

The production rates of many potential oxide (MO^{+}/M^{+}) and argide (MAr^{+}/M^{+}) interferences were determined from tests conducted on the NIST reference standards SRM 1158 and SRM 611. Using SRM 1158, which has high Ni and Cu but very low PGE abundances, the production rate of $NiAr^{+}$ and $CuAr^{+}$, which interfere at ^{101}Ru and ^{105}Pd, respectively, were both determined to be $MAr^{+}/M^{+} \approx 8x10^{-5}$ (Table 9). SRM 611 has many lithophile elements doped to ~500 ppm levels, but has negligibly low Ru, Os, and Ir contents. In the limiting assumption that all blank-corrected signals measured at masses corresponding to these elements in SRM 611 are produced by oxide and/or argide interferences, upper limits were placed on MO^{+}/M^{+} and MAr^{+}/M^{+} production rates, and these are listed in Table 9. The Pd abundance of SRM 611 is non-neglible (Sylvester and Eggins, 1997) but still permitted an upper limit of $^{89}Y^{16}O$ production to be determined based on the excess ^{105}Pd compared to other Pd masses (Table 9). It was previously known that oxide interferences in LA-ICP-MS are much lower than those in solution nebulization ICP-MS, due to the lack of a solution matrix (Sylvester and Eggins,1997). Based on the trace element abundances of the natural ankaramite starting material (Chen et al., 1991) and the oxide/argide production rates shown in Table 9, the interferences on ^{101}Ru, ^{105}Pd, and ^{193}Ir are de-

termined to be <1% of the magnitude of the LA-ICP-MS analyses reported in this study, and usually much smaller. Under the further assumption that oxide and argide interferences on ^{187}Re, ^{195}Pt, and ^{197}Au have production rates comparable to those in Table 9, molecular interferences on Re, Pt, and Au in this study are also considered to be negligible.

The LA-ICP-MS intensities were internally standardized against Mg or Fe, which were independently determined by electron microprobe. Instrumental sensitivity factors for each isotope monitored relative to ^{25}Mg or ^{57}Fe were determined by measuring signal intensity from the standard NIST silicate glass SRM 612, which has known concentrations of the elements of interest (Pearce et al., 1997; Sylvester and Eggins, 1997). This standard does not contain usable levels of some elements (Ru, Os, Ir), and in these cases metal from the iron meteorite Hoba was used as a standard (Campbell et al., 2002). Although the difference between the silicate samples and this metal standard may introduce modest systematic errors in the absolute abundances measured for these elements, these should cancel out in the calculation of the partition coefficients determined in this study. In most experiments, multiple LA-ICP-MS measurements of each phase were performed, and the quoted uncertainty refers to the standard error (1 sigma) of the mean of 3 to 5 analyses of each phase. In other experiments only a single analysis was performed on each phase, and the uncertainties were calculated from counting statistics as well as an instrumental error that is largely due to the transience of the signal. The counting errors incorporate both the measured counts and the counts in the blank measurement. The instrumental error was calculated from repeat measurements of the standards, by stripping away the statistical (counting) variance from the variance of the standard analyses. This is a conservative estimate of the instrumental error because it assumes homogeneity in the standards, which are known to have fine scale heterogene-

ities. Instrumental errors (1□) were typically ~4% (Table 8).

Results

Equilibrium

Attainment of equilibrium can be checked by use of the olivine-liquid equilibrium:

$$2FeO + Mg_2SiO_4 = 2MgO + Fe_2SiO_4. \qquad \text{(eq. 1)}$$
$$\text{(liquid)} \quad \text{(olivine)} \quad \text{(liquid)} \quad \text{(olivine)}$$

Olivine compositions produced in a subset of runs (see Tables 2 and 5) are in good agreement with the compositions predicted by estimating X_{FeO} in the silicate liquid as a function of temperature and oxygen fugacity, using the expression in Kress and Carmichael (1991), and the predictive equation of Snyder and Carmichael (1992). Chromites produced in most experiments were slightly zoned from core to rim in terms of FeO, Cr_2O_3 and MgO, but this is thought to have only a small effect on equilibrium partitioning of the HSE. With the exception of the Ir-bearing experiments, concentrations of HSE in both the crystals and glasses were nearly homogeneous and reproducible (Tables 7 and 8).

HSE solubility in silicate glasses

Many previous studies of HSE partitioning have encountered a problem with submicroscopic metallic flakes interfering with analyses of glasses, especially when experimental oxygen fugacities were low (e.g., Borisov and Palme, 1996; Walter et al., 2000). As noted above, the relatively high oxygen fugacities at which our experiments were conducted were chosen to circumvent the

formation of such metallic flakes. Additionally, the LA-ICP-MS signal was monitored for "spikes" that would indicate the presence of HSE-rich nuggets. Conditions fostering the stability of nuggets should not be confused with conditions of metal saturation. For example, both run products shown in Figure 2 are from runs carried out at Ru metal saturation, but at an oxygen fugacity higher than where Ru-rich micro-nuggets have been reported. For experiments that were saturated with a metal phase, we can compare our HSE solubilities to those of previous studies.

Rhenium concentrations in some of the glasses are high, but still in agreement with previous work on Re solubility. For example, the work of both Ertel et al. (2001) and Righter and Drake (1997) shows that wt% levels of Re_2O_3 (0.1 to 3.0 wt%) are expected at high oxygen fugacities. As the present experiments were not saturated with either Re or a Re-oxide, the Re concentrations in the glass are variable and do not correlate with oxygen fugacity. The valence of Re may be 3+ or 4+ as suggested by its compatibility in spinels (Righter and Downs, 2001), or it may be higher, as suggested by its solubility in silicate melt as a function of fO_2 (Ertel et al., 2001). Glass from experiment 158A at the HM buffer and 1300 ˚C contained 17 ppm Au and 82 ppm Pd (Table 8). These values are in agreement with the study of Borisov and Palme (1996) who measured between 10 - 20 ppm Au, and 70 to 90 ppm Pd in silicate melts, under similar T-X-fO_2 conditions. The nugget effect for both of these elements appears at much lower oxygen fugacities, near the IW buffer.

Rhodium concentrations in glasses from this study range from 5 to 12 ppm (Table 7), and these are in agreement with concentrations measured by Ertel et al. (1999) in glasses that were equilibrated with PtRh metal at 1300 ˚C and similar oxygen fugacities. Borisov and Nachtweyh (1998) found that Ru dissolves in CMAS composition silicate melt at concentrations between 1 and 100 ppm in the oxidized region, similar to the range measured in glasses in this study (1 to 120 ppm; Table 7 and 8). Finally, the very low Ir concentrations measured in our experimental glasses (20 ppb to ~ 10,000 ppb) are as expected from previous work by Borisov and Palme (1995) who found that Ir solubility increased from 10 to 10,000 ppb at fO_2 from 10^{-4} to 10^{-1}. In summary, all of the concentrations of HSEs in glasses measured here are at levels that are consistent with previous work carried out under similar oxygen fugacities. This, together with the absence of "spikes" in the LA-ICP-MS analyses, lead us to the conclusion that the glasses are free of metal micro- or nano-nuggets.

Discussion

Spinel/melt partition coefficients

The partition coefficients for Re determined here are all lower than unity, indicating that Re is incompatible in Cr-rich spinel. There is no systematic dependence upon oxygen fugacity as might be expected due to possible valence changes in Re from 3+ to 4+ to 6+ as oxidized conditions are attained (Fig. 4). However, the variations in D(Re) appear to be a function of the Re content of the spinel, within the 1 bar series of experiments (where Re contents vary from 1 ppm to > 100 ppm), but results from higher pressure experiments do not follow that trend (Fig. 4). These values are all much lower than the upper bounds reported by Sattari et al. (2002), in which

it was unclear if Re was compatible or incompatible in spinels. Regardless of what is causing the variation in D(Re) spinel/melt in this study, all results indicate incompatibility.

Chromite/melt partition coefficients for Au and Pd determined here are 0.076 and 0.14, respectively, showing clear incompatibility in Cr-rich spinel. This might be expected since both elements have a valence of 1+ in silicate melts (Borisov and Palme, 1996). Capobianco et al. (1994) also report the incompatibility of Pd in magnetite-rich spinels, and Mitchell and Keays (1981) report low Pd concentrations in spinel mineral separates from spinel peridotites. The D(Pd) chromite/melt of 1.60 reported by Puchtel and Humayun (2001), based on measurements of mineral separates from komatiitic basalts from the Vetreny Belt, could be attributed to the presence of Pd-rich sulfide inclusions in the chromite, or perhaps another minor Pd-rich phase.

Rhodium has previously been shown to be compatible in inverse spinels such as magnetite and normal spinels such as $MgAl_2O_4$ (Capobianco et al., 1994; Capobianco and Drake, 1990; Fig. 5), with D(Rh) ranging from 90 to 400. The results of this study show that addition of Cr-bearing components does not change the compatible nature of Rh—the range from this study is 40 to 500 (Fig. 5). The latter high values are from spinels with an inverse structure, and it is possible that inverse spinels show a greater affinity for Rh than do normal spinels. On the other hand, the highest D(Rh) spinel/melt values are from those experiments with the highest concentrations of Rh (Fig. 5); if non-Henrian effects observed for Ni, Co and V (Righter, 2002) are also true for Rh, then the high D values could be attributed to the high concentrations in the spinels. Finally, a slight increase of D(Rh) with increasing fO_2 may be attributed to a change in valence of Rh, but this should be confirmed by future studies. For the purposes of modelling natural suites below, a value of D(Rh) spinel/melt = 75 is used, derived from the most reduced experiments

containing Cr-bearing spinel.

Ruthenium has also previously been shown to be highly compatible in studies of experimental inverse spinels such as magnetite and experimental normal spinels such as $MgAl_2O_4$ (Capobianco et al., 1994; Capobianco and Drake, 1990; Fig. 6), and in measurements of mineral separates from komatiitic basalts from the Vetreny Belt (D(Ru) chromite/melt = 151; Puchtel and Humayun, 2001). The results of this study show that while addition of Cr-bearing components does not change the compatible nature of Ru, comparison of D(Ru) at the same temperature and oxygen fugacity reveals that Cr-bearing spinels always have lower D(Ru) than magnetite. This indicates that inverse spinels have a greater affinity for Ru than normal spinels. The runs at lowest oxygen fugacity have the highest value, suggesting there might be a valence change in Ru from 4+ to 3+ across this fO_2 range (Fig. 6). In addition, within the data sets of Capobianco et al. (1994) and Capobianco and Drake (1990), there is a trend of increasing D(Ru) spinel/melt with increasing Ru concentration in the spinel. If non-Henrian effects observed for Ni, Co and V (Righter, 2002) are also true for Ru, then the high D values could be attributed to high Ru concentrations in the spinels. Finally, one of the runs (# 158A) was analyzed by both SIMS and LA-ICP-MS and although there are differences in the absolute numbers, the agreement in D(Ru) is very good (Tables 7 and 8). For the purposes of modelling natural suites below, a value of D(Ru) spinel/melt = 1000 is used, again, derived from the most reduced experiments, and those with Cr-bearing spinel.

Iridium solubility in glasses is very low and was only measurable in two runs. In one of these, the variation in Ir contents in both the spinel and the glass is quite high (Table 8) indicating that equilibrium may not have been attained. Nonetheless, it is clear that D(Ir) is high and Ir is very compatible in Cr-bearing spinels. Compatibility of Ir and Os in spinel was also proposed by

Puchtel and Humayun (2001), based on in measurements of mineral separates from komatiitic basalts from the Vetreny Belt (D(Ir) chromite/melt = 100). Future work should address the effect of changing valence of Ir from 2+ to 4+. As the range of D(Ir) spinel/melt in Table 8 is large, for the purposes of modelling natural suites below a range of D(Ir) spinel/melt values is used, from 200 to 2000.

Olivine/melt and pyroxene/melt partition coefficients

Rhenium, Pd and Au are all incompatible in olivine, with values between 0.01 and 0.12 (Table 8). The low values for D(Re) overlap those found in earlier studies (~0.01) by Righter et al. (2000). This is supported by the general trends of increasing concentration of all three elements with fractionation or differentiation. For example, the MORB suites considered below exhibit increasing Re, Pd and Au with decreasing MgO, Ni or Cr. In addition, Puchtel and Humayun (2001) reported a D(Pd) olivine/melt of 0.03, based on measurements of olivine separates from komatiitic basalt from the Vetreny Belt. For the purposes of modelling olivine-bearing natural suites below, we use values of 0.1 for D(Au) and D(Pd) and 0.01 for D(Re).

The value of D(Ru) olivine/melt measured here (0.23; Table 8) is in agreement with work reported by Capobianco et al. (1991), where Ru is incompatible (0.2 to 0.8), and is temperature dependent. However, the value measured here is lower than values reported by Brenan et al. (2002), and this is due to decreasing D(Ru) olivine/melt with increasing fO_2. Our low value of 0.23 falls at a higher fO_2 (HM) than the range they measured from 0.6 (QFM+4) to 2.2 (QFM+1). This trend is presumably reflecting the increasing valence of Ru from 3+ to 4+ as oxygen fugacity increases. Thus, in natural systems, where oxygen fugacity is closer to QFM, Ru will be more compatible in olivine (e.g., D(Ru) = 1.7 in Puchtel and Humayun, 2001), and we

choose a value of 1 for D(Ru).

Clinopyroxene is a significant host phase for several HSE. Our results here show that Pt is mildly compatible in clinopyroxene, with a D(Pt) = 1.5. Recent work by Hill et al. (2000) shows that Ru is also mildly compatible in clinopyroxene, with a strong dependence upon Ca-Tschermak's component. Rhenium is incompatible in clinopyroxene and orthopyroxene, with D's < 0.2, in agreement with the results of Watson et al. (1987) of D(Re) clinopyroxene/melt = 0.05 (experiments carried out in air), and results of Righter and Hauri (1998) of D(Re) orthopyroxene/melt = 0.18 (experiments carried out near QFM buffer).

HSE behavior during differentiation of basic magmas

Positive correlations between Ni or Cr and PGEs such as Ru, Os and Ir in basaltic rock suites suggest that the latter three PGEs are compatible in spinels. However, because many basic rocks suites are sulfide saturated, and sulfide is a major control of Re and PGE concentrations, the role of sulfide must be better defined to interpret such trends. As a result, the role of chromite can be best defined in suites that are sulfide under-saturated, which can be determined by examining total S and PGE contents of the silicate melts. With this approach in mind, we will illustrate that Re is incompatible and Ir, Ru and Rh are compatible in spinels, by utilizing the results of these experiments and applying them to several natural basaltic or ultrabasic rock suites. Major elements in a given suite were modeled using the MELTS computer application (Ghiorso and Sack, 1994), and the amount of spinel or chromite involved in the fractionation is defined by fitting Cr-MgO trends in a given suite. The HSE spinel/melt partition coefficients determined here, together with partition coefficient data for olivine and pyroxene, are then used to evaluate the role of spinel in controlling HSE concentrations in these suites.

The evolution of the Kostomuksha komatiite suite is characterized by liquidus olivine across a large composition range (40 to 24 wt. % MgO; Fig. 7). Chromite does not stabilize until the liquid has ~ 24 wt% MgO, and the suite is sulfide-undersaturated (Puchtel and Humayun, 2000). Thus any compositional variation in trace elements can be attributed entirely to olivine fractionation. A Rayleigh fractionation model can adequately reproduce the trends if Pd is highly incompatible in olivine and Ru is mildly compatible. The former is supported by our new data, and the latter by the results of Brenan et al. (2002).

The Vetreny Belt komatiitic basalt lava lake has olivine and chromite as liquidus phases across a wide temperature interval (Puchtel and Humayun, 2001), thus allowing an assessment of the role of chromite in the fractionation of Ru and Ir (Fig. 8). As with the Kostomuksha komatiites, the Vetreny belt samples are not sulfide saturated because Cu, Pd and Pt exhibit incompatible behavior within this interval of the fractionation series; thus sulfide does not play a role in the fractionation. Crystallization of olivine alone cannot reproduce the trends of Ru and Ir with Cr or MgO (Fig. 8). Instead, Cr-rich spinel fractionation is required to lower the Ru and Ir values in the more evolved samples. The rock analyses are well fit using D(Ir) spinel/melt ~ 2000 and D(Ru) spinel/melt = 1000, in agreement with the range of D's measured in our study. It should be noted, however, that Puchtel and Humayun (2001) obtained an empirical D(Ir)=100 and D(Ru)=150 from a chromite separate from a Vetreny cumulate komatiite, and using these lower D values could not account for the fractionation of Ru or Ir by olivine+chromite alone. The inverse correlation of D(Ru) in spinel with log fO_2 implies that the applicable D(Ru) for a natural magma should be higher than the empirical value obtained. The discrepancy remains to be resolved.

Komatiitic basalts from the Cape Smith Fold Belt, Quebec, have been analyzed for HSE's by Barnes and Picard (1993). Trends of Cr, Pt, Pd, Rh, Ir and MgO demonstrate the compatible nature of Ir and Rh, and the incompatible nature of Pd and Pt during differentiation of this suite (Fig. 9). The high initial Pd and Pt contents indicate that these magmas were sulfide undersaturated, and remained so until lower MgO contents, where concentrations of all HSE's begin to drop off rapidly. The lower Ir contents compared to Rh in the more evolved samples indicate that Ir is more compatible in spinel than Rh, consistent with our partitioning results where D(Ir) spinel/melt > D(Rh) spinel/melt (Fig. 9). Partition coefficients required to successfully model these komatiites compare well with our measurements. The general observation that D(Ir), D(Os) and D(Ru) are all likely to be higher than D(Rh) spinel/melt was also made by Capobianco et al. (1994).

The incompatibility of Re in spinel and olivine is illustrated in data from the Hawaiian Scientific Drilling Project (HSDP; Fig. 10; Hauri et al., 1996; Rhodes, 1996). Re increases as Ni decreases due to fractionation of olivine and spinel; the fractionation of olivine and spinel from a basaltic parent decreases Ni due to its compatibility in olivine and spinel (Schilling et al., 1983; Righter, 2002). As Re is incompatible in olivine and spinel, the concentrations will increase during fractionation. The slope of the fractionation vector in Figure 10 is similar to the trend of the HSDP Re-Ni data, indicating that variations in these elements can be due largely to fractionation. Analyses of olivine and spinel mineral separates from komatiitic rocks also indicate Re is incompatible in both phases (Walker et al, 1999).

While our measurements of D(Re) spinel/melt shows incompatibility, there are some spinel

compositions showing opposite behavior. The suite from Volcan Alcedo in the Galapagos Islands (Righter et al., 1998) initially shows an increase in Re with decreasing Ni content and can be modeled by co-fractionation of olivine, cpx, and plag. When Ti-magnetite joins this assemblage, Re begins to decrease in the residual melt, indicating compatibility of Re in this spinel. This may relate to the Ti content or the relatively low oxygen fugacity represented by this rock suite, where Re may be reduced to a valence more compatible in the crystallizing assemblage.

The partitioning results presented here for chromite and olivine demonstrate that HSEs can be fractionated during differentiation. Fractionation of olivine and chromite, both of which will concentrate Rh, Ir, and Ru, but not Pd or Au, can lead to HSE patterns very different from the parent magma. Thus, elevated Pd/Ir, Au/Ir, and Pd/Ru ratios in differentiated basalts can be attributed both to olivine and chromite fractionation (as suggested by Capobianco et al., 1991), and to lowered solubility of Ru and the IPGEs with changing melt composition during fractionation (Capobianco et al. 1994). Both of these effects are observed in the natural sample suites discussed above.

Pt and Re in planetary mantles

The similar concentrations of Pt in terrestrial basalts and peridotite, and in martian basaltic shergottites and clinopyroxenites (Jones et al., 2003) suggests that Pt has a bulk partition coefficient of approximately 1 during mantle melting. The fact that Pt is mildly compatible in clinopyroxene (this study), coupled with its compatibility in sulfide (Fleet et al., 1991, 1996), can explain this behavior, especially for the martian nakhlites, because nakhlites contain 80-90% clinopyroxene and also contain sulfide (Bunch and Reid, 1975). If the nakhlites crystallized from a basaltic parent magma, and the bulk D is close to unity, then Pt concentrations will be similar in

the parent melt and the cumulates. In contrast, when considering more basic and ultrabasic systems, where the percentage of melting is higher (removing cpx and sulfide from the residue), a bulk D(Pt) < 1 would be expected since Pt is incompatible in chromite and olivine. This has been demonstrated for sulfide-undersaturated komatiitic and komatiitic basalt suites analyzed by Puchtel and Humayun (2000, 2001), where D(Pt) bulk = 0.52-0.53.

Finally, work by Brandon et al. (1998, 1999) has shown that radiogenic ^{186}Os and ^{187}Os measured in Hawaiian basalts could be explained by mixing of a high Pt/Re and high Os material into the source region of these basalts. Such a material would need enough Pt to elevate the Pt/Re ratio, and enough Os to have an effect on the high Os mantle into which it would be mixed. Addition of high Os and high Pt/Os outer core metal to the mantle meets these requirements (e.g., Brandon et al., 1998, 1999). An explanation due to crustal recycling, however, may be considered because our results show that a clinopyroxene-rich rock could have an unusually high Pt/Re ratio, based on the partition coefficients for clinopyroxene determined here. Furthermore, if a clinopyroxene-rich and sulfide-rich rock were involved, it would be possible to create an even higher Pt/Re ratio, because D(Pt) sulfide/melt > D(Re) sulfide/melt (Fleet et al., 1996; Jones and Drake, 1986; Roy-Barman et al., 1998). Quantitative evaluation of such a crustal recycling scenario, however, is problematic for several reasons. First, the few eclogites that have been analyzed have low Os concentrations (e.g., Esperanca et al., 1997; Becker, 2000), although there are some as high as typical mantle (e.g., Pearson et al., 1995). Second, many eclogite or clinopyroxenite samples have not been analyzed simultaneously for Pt, Os and Re all together. Whether recycled clinopyroxenite or eclogite would have a high enough Pt/Re ratio and Os concentration to account for the Os isotopic trends reported by Brandon et al. (1998, 1999) awaits further

evaluation.

Future

As spinel chemistry changes dramatically within a differentiation series, so will the partition coefficients. The combined effects of temperature, oxygen fugacity and spinel chemistry must ultimately be evaluated for Re, Os, Ir and other HSEs. The role of such factors will have to be distinguished from other factors such as valence, crystal chemistry, variations in the HSE concentrations in the spinels, melt composition, and sulfide and alloy distribution coefficients and saturation. This study has demonstrated that Cr-rich spinels can be significant hosts for Rh, Ru and Ir. The incompatibility of Pd and Au in spinel and olivine, and the mild compatibility of Pt in clinopyroxene is also significant and will aid in our interpretation of HSE contents of basaltic rocks.

Acknowledgements

This research is supported by NSF grant EAR-0074036 (KR), EAR-0309786 (MH) and by NASA NAG5-13133 (MH). Y. Guan provided assistance with some of the SIMS work at ASU. Electron microprobe analysis was facilitated by K. Domanik at the University of Arizona and C. Schwandt and L. Le at the Johnson Space Center. Discussions with A. Brandon, J. Jones, R. Nielsen, C. Capobianco, and M. Drake influenced this work. The reviews of M. Horan, C. Neal, and M. Norman improved the clarity of the manuscript.

References

Agiorgitis, G. and R. Wolf (1978) Aspects of osmium, ruthenium and iridium contents in some Greek chromites. *Chem. Geol.* **23**, 267-272.

Auge, T. (1988) Platinum-group minerals in the Tiebaghi and Vourinos Ophilitic Complexes: Genetic implications. *Can. Mineral.* **26**, 177-192.

Barnes, S.-J. and Picard, C.P., 1993. The behavior of platinum-group elements during partialmelting, crystal fractionation, and sulphide segregation: an example from the Cape Smith Fold Belt, northern Quebec. *Geochim. Cosmochim. Acta* **57**, 79-87.

Becker, H. (2000) Re-Os fractionation in eclogites and blueschists and the implications for recycling of oceanic crust into the mantle. *Earth Planet Sci. Lett.* **177,** 287-300.

Borisov A. and Palme H. (1995) The solubility of iridium in silicate melts: New data from experiments with $Ir_{10}Pt_{90}$ alloys. *Geochim. Cosmochim. Acta* **59**, 481-485.

Borisov, A. and H. Palme (1996) Experimental determination of the solubility of Au in silicate melts. *Mineral. Petrol.* **56**, 297-312.

Borisov, A. and Nachtweyh, K. (1998) Ru solubility in silicate melts: experimental results in oxidizing region. *Lunar. Planet. Sci.* **XXIX**, abstract #1320.

Brandon, A., Walker, R.J., Morgan, J.W., Norman, M.D. and Prichard, H.M. (1998) Coupled ^{186}Os and ^{187}Os evidence for core-mantle interaction. *Science* **280**, 1570-1573.

Brandon, A., Norman, M.D., Walker, R.J., and Morgan, J.W. (1999) ^{186}Os / ^{187}Os systematics of Hawaiian picrites. *Earth Planet Sci. Lett.* **174,** 25-42.

Brenan, J.M., Dalpe, C. and McDonough, W.F. (2002) PGE's are fractionated by olivine-melt partitioning. Goldschmidt Conference Abstracts, Davos, Switzerland, A103.

Brenan, J.M., McDonough, and W.F. Dalpe, C. (2003) Experimental constraints on the partitioning of rhenium and some platinum-group elements between olivine and silicate melt. *Earth Planet. Sci. Lett.* 212, 135-150.

Brügmann, G. E., Arndt, N. T., Hofmann, A.W., and Tobschall, H.J. (1987) Noble metal abundances in komatiite suites from Alexo, Ontario, and Gorgona Island, Colombia. *Geochim. Cosmochim. Acta* **51**, 2159-2169.

Bunch, T.E., and A.M. Reid (1975) The Nakhlites Part I: Petrography and mineral chemistry. *Meteoritics* **10**, 303-315.

Campbell A. J. and Humayun M. (1999) Trace element microanalysis in iron meteorites by laser ablation ICPMS. *Anal. Chem.* **71**, 939-946.

Campbell A. J., Humayun M. and Weisberg M. K. (2002) Siderophile element constraints on the formation of metal in the metal-rich chondrites Bencubbin, Weatherford, and Gujba. *Geochim. Cosmochim. Acta* **66**, 647-660.

Capobianco, C. J. (1993). On the thermal decomposition of $MgRh_2O_4$ spinel and the solid solution $Mg(Rh, Al)_2O_4$. *Thermochimica Acta* **220**, 7-16.

Capobianco, C. J. (1998) Ruthenium solubility in hematite. *American Mineralogist* **83**, 1152-1160.

Capobianco, C. J. and M. J. Drake (1990) Partitioning of ruthenium, rhodium, and palladium between spinel and silicate melt and implications for platinum group element fractionation trends. *Geochim. Cosmochim. Acta* **54**, 869-874.

Capobianco, C. J., M.J. Drake, and Rogers, P.S.Z (1991) Crystal/melt partitioning of Ru, Rh and Pd for silicate and oxide phases. *Lunar Planet. Sci.* **XXII**, 179-180.

Capobianco, C. J., R. L. Hervig and M.J. Drake (1994) Experiments on crystal/liquid partitioning of Ru, Rh and Pd for magnetite and hematite solid solutions crystallized from silicate melt. *Chemical Geology* **113**, 23-43.

Carmichael, I.S.E. (1967) Iron-titanium oxides and oxygen fugacities in volcanic rocks. *J. Geophys. Res.* **72**, 4665-4687.

Carmichael, I.S.E. (1991) The redox states of basic and silicic magmas: a reflection of their source regions? *Contrib. Mineral. Petrol.* **106**, 129-141.

Chen, C.Y., Frey, F.A., Garcia, M.O., Dalrymple, G.B., and Hart, S.R. (1991) The tholeiite to alkalic basalt transition at Haleakala Volcano, Maui, Hawaii. Contrib, Mineral. Petrol. 106, 183-200.

Ertel, W., O'Neill, H.St.C., Sylvester, P.J. and Dingwell, D.B. (1999) Solubilities of Pt and Rh in a haplobasaltic silicate melt at 1300 ˚C. *Geochim. Cosmochim. Acta* **63**, 2439-2449.

Ertel, W., O'Neill, H.St.C., Sylvester, P.J., Dingwell, D.B. and B. Spettel (2001) The solubility of rhenium in silicate melts: Implications for the geochemical properties of rhenium at high temperatures, *Geochim. Cosmochim. Acta* **65**, 2161-2170.

Esperanca, S., Carlsn, R.W., Shirey, S.B., and Smith, D. (1997) Dating crust-mantle separation: Re-Os isotopic study of mafic xenoliths from central Arizona. *Geology* **25**, 651-654.

Fleet, M. E., Stone, W. E. and Crocket, J. H. (1991) Partitioning of palladium, iridium, and platinum between sulfide liquid and basalt melt: Effects of melt composition, concentration, and oxygen fugacity. *Geochim. Cosmochim. Acta* **55**, 2545-2554.

Fleet, M. E., Crocket, J. H. and Stone, W.E. (1996) Partitioning of platinum-group elements (Os, Ir, Ru, Pt, Pd) and gold between sulfide liquid and basalt melt. *Geochim. Cosmochim. Acta* **60**, 2397-2412.

Ghiorso M. S. and Sack R. O. (1994) Chemical mass transfer in magmatic processes IV. A revised an internally consistent thermodynamic model for the interpolation and extrapolation of liquid-solid equilibria in magmatic systems at elevated temperatures and pressures. *Contrib. Mineral. Petrol.* **119**, 197-212.

Green T.H. (1994) Experimental studies of trace element partitioning applicable to igneous petrogenesis — Sedona 16 years later. *Chem. Geol.* **117**, 1-36.

Hauri, E.H., Lassiter, J.L. and DePaolo, D.J. (1996) Osmium isotope systematics of drilled lavas from Mauna Loa, Hawaii. *Jour. Geophys. Res.* **101**, 11701-11713.

Hill, E., Wood, B.J., and Blundy, J.D. (2000) The effect of Ca-Tschermaks component on trace element partitioning between clinopyroxene and silicate melt. *Lithos* **53**, 203-215.

Irving, A.J. (1978) A review of experimental studies of crystal/liquid trace element partitioning. *Geochim. Cosmochim. Acta* **42**, 743-770.

Jones, J.H., and M.J. Drake (1986) Geochemical constraints on core formation in the Earth. *Nature* **322**, 221-228.

Jones, J.H., Neal. C.R. and Ely, J.C. (2003) Signatures of the highly siderophile elements in the SNC meteorites and Mars: a review and petrologic synthesis. *Chem. Geol.* **196**, 21-41.

Kress, V.C. and Carmichael, I.S.E. (1991). The compressibility of silicate liquids containing Fe_2O_3 and the effect of composition, temperature, oxygen fugacity and pressure on their redox states. *Contrib. Mineral. Petrol.* **108**, 82-92.

Krutzsch, B. and S. Kemmler-Sack (1983) Sauerstoff - Spinelle mit ruthenium und iridium. *Materials Research Bulletin* **18**, 647-652.

Lindstrom, D.J. and Jones, J.H. (1996) Neutron activation analysis of multiple 10-100 mg glass samples from siderophile element partitioning experiments. *Geochim. Cosmochim. Acta* **60**, 1195-1203.

Mitchell, R.H. and Keays, R.R. (1981) Abundance and distribution of gold, palladium and iridium in some spinel and garnet lherzolites: implications for the nature and origin of precious metal-rich intergranular components in the upper mantle. *Geochim. Cosmochim. Acta* **45**, 2425-2442.

Myers, J. and Eugster, H.P. (1983) The system Fe-Si-O; oxygen buffer calibrations to 1,500 K. *Contrib. Mineral. Petrol.* **82**, 75-90.

O'Neill, H. St. C. and Nell, J. (1997) Gibbs free energies of formation of RuO_2, IrO_2, and OsO_2: A high-temperature electrochemical and calorimetric study. *Geochim. Cosmochim. Acta* **61**, 5279-5293.

O'Neill, H.St.C. and Pownceby, M.I. (1993a) Thermodynamic data from redox reactions at high temperatures. I. An experimental and theoretical assessment of the electrochemical method using stabilized zirconia electrolytes, with revised values for the Fe-"FeO", Co-CoO, Ni-NiO and Cu-Cu_2O oxygen buffers, and new data for the W-WO2 buffer. *Contrib. Mineral. Petrol.* **114**, 296-314.

O'Neill, H.St.C. and Pownceby, M.I. (1993b) Thermodynamic data from redox reactions at high temperatures. II. The MnO-Mn_3O_4 oxygen buffer and implications for the thermodynamic properties of MnO and Mn_3O_4. *Contrib. Mineral. Petrol.* **114**, 315-320.

Page, N. J. (1984) Palladium, platinum, rhodium, ruthenium and iridium in peridotites and chromitites from ophiolite complexes in Newfoundland. *Can. Mineral.* **22**, 137-149.

Parry, S. J. (1984). Abundance and distribution of palladium, platinum, iridium and gold in some oxide minerals. *Chem. Geol.* **43**, 115-125.

Pearce N. J. G., Perkins W. T., Westgate J. A., Gorton M. P., Jackson S. E., Neal C. R. and Chenery S. P. (1997) A compilation of new and published major and trace element data for NIST SRM 610 and NIST SRM 612 glass reference materials. *Geostandards Newslett.* **21**, 115-144.

Pearson, D.G., Snyder, G.A., Shirey, S.B., Taylor, L.A., Carlson, R.W. and Sobolev, N.V. (1995) Archaean Re-Os age for Siberian eclogites and constraints on Archaean tectonics. *Nature* **374**, 711-714.

Pouchou, J.-L. and Pichoir, F. (1991) Quantitative analysis of homogeneous or stratified micro-volumes applying the model "PAP". In K.F.J. Heinrich and D.E. Newbury, eds., Electron Microprobe Quantitation. Plenum Press, New York, 31-75.

Pownceby, M.I. and O'Neill, H. St. C. (1994) Thermodynamic data from redox reactions at high temperatures. IV. Calibration of the Re-ReO_2 oxygen buffer from EMF and NiO+Ni-Pd redox sensor measurements. *Contrib. Mineral. Petrol.* **118**, 130-137.

Puchtel I. and Humayun, M. (2000) Platinum group elements in Kostomuksha komatiites and basalts: implications for oceanic crust recycling and core-mantle interaction, *Geochim. Cosmochim. Acta* **64**, 4227-4242.

Puchtel I. and Humayun, M. (2001) Platinum group element fractionation in a komatiitic basalt lava lake, *Geochim. Cosmochim. Acta* **65**, 2979-2993.

Puchtel I.S., Brügmann, and Hofmann, A.W. (1998) Precise Re-Os mineral isochron and Pb-Nd-Os isotope systematics of a mafic-ultramafic sill in the 2.0 Ga Onega plateau (Baltic Shield). *Earth Planet Sci. Lett.* **170,** 447-461.

Razin, L. V. and G. A. Khomenko (1969) Accumulation of osmium, ruthenium, and the other platinum-group metals in chrome spinel in platinum-bearing dunites. *Geokhimiya(No.**6**)*: 659-672.

Rhodes, J.M. (1996) Geochemical stratigraphy of lava flows sampled by the Hawaiian Scientific Drilling Project. *Jour. Geophys. Res.* **101**, 11722-42.

Righter, K. (2002) Nickel and cobalt partitioning between spinel and basaltic melt: applications to planetary basalt suites. Lunar Planet. Sci. XXXIII, abstract 1253 [CD-ROM].

Righter, K. and R.T. Downs (2001) Crystal structures of Re- and PGE-bearing magnesioferrite spinels: implications for accretion, impacts and the deep mantle. *Geophysical Research Letters* **28**, 619-622.

Righter, K. and E. H. Hauri (1998) Compatibility of Rhenium in Garnet During Mantle Melting and Magma Genesis. *Science* **280**, 1737-1741.

Righter K, and Drake MJ. (1997) Metal-silicate equilibrium in a homogeneously accreting Earth: new results for Re. *Earth Planet. Sci. Lett.***146**, 541-53.

Righter, K., Walker, R.J. and Warren, P.W. (2000) The origin and significance of highly siderophile elements in the lunar and terrestrial mantles. in (R.M. Canup and K. Righter, eds.) *Origin of the Earth and Moon*, Univ. of Arizona Press, Tucson, 291-322.

Righter, K., Chesley, J.T., Geist, D. and Ruiz, J. (1998) Behavior of Re during magma fractionation: an example from Volcan Alcedo, Galapagos Archipelago. *J. Petrol.* **39**, 785-795.

Roeder, P.L. and Reynolds, I. (1991) Crystallization of chromite and chromium solubility in basaltic melts. *J. Petrol.* **32**, 909-934.

Roy-Barman, M., Wasserburg, G. J., Papanastassiou, D.A., and Chaussidon, M. (1998) Osmium isotopic compositions and Re-Os concentrations in sulfide globules from basaltic glasses. *Earth Planet Sci. Lett.* **154***:* 331-347.

Sattari, P., Brenan, J.M., Horn, I. And McDonough, W.F. (2002) Experimental constraints on the sulfide- and chromite-silicate melt partitioning behavior of Re and platinum group elements. *Econ. Geol.* **97**, 385-398.

Schilling, J.-G., Zajac, M., Evans, R., Johnston, T., White, W., Devine, J.D. and Kingsley, R. (1983) Petrologic and geochemical variations along the mid-Atlantic Ridge from 29° to 73° N. *Amer. Jour. Sci.* **283**, 510-586.

Schwandt, C. S. and McKay, G.A. (1998) Rare earth element partition coefficients from enstatite/melt synthesis experiments. *Geochim. Cosmochim. Acta* **62**, 2845-2848.

Snyder, D.A. and Carmichael, I.S.E. (1992) Olivine-liquid equilibria and the chemical activities of FeO, NiO, Fe_2O_3, and MgO in natural basic melts, *Geochim. Cosmochim. Acta* **56**, 303-318.

Stolper, E. (1977) Experimental petrology of eucritic meteorites. *Geochim. Cosmochim. Acta* **41**, 587-611.

Sylvester P. J. and Eggins S. M. (1997) Analysis of Re, Au, Pd, Pt and Rh in NIST glass certified reference materials and natural basalt glasses by laser ablation ICP-MS. *Geostandards Newslett.* **21**, 215-229.

Walker, R. J., Storey, M., Kerr, A.C., Tarnet, J. and Arndt, N.T. (1999) Implications of ^{187}Os isotopic heterogeneities in a mantle plume: evidence from Gorgona Island and Curacao. *Geochim. Cosmochim. Acta* **63**, 713-728.

Walter MJ, Newsom H, Ertel W, Holzheid A. 2000. Siderophile elements in the Earth and Moon: metal/silicate partitioning and implications for core formation. In (Canup RM, Righter K, ed.) *Origin of the Earth and Moon.* Univ. Arizona Press, Tucson, pp. 265-90.

Watson, E.B., BenOthman, D., Luck, J.-M., and Hofmann, A.W. (1987) Partitioning of U, Pb, Cs, Yb, Hf, Re, and Os between chromian diopsidic pyroxene and haplobasaltic liquid. *Chem. Geol.* 62, 191-208.

Table 1: Chemical analyses of starting materials

run	SiO_2	TiO_2	Al_2O_3	Cr_2O_3	FeO*	MnO	MgO	CaO	Na_2O	K_2O	P_2O_5	Total
Ank.	43.66	2.97	13.13	-	14.84	0.21	9.75	12.12	2.5	0.86	0.37	100.41
Euc.	50.0	-	13.0	-	19.0	-	7.0	11.0	-	-	-	100.0
DiAn	50.3	-	15.4	-	-	-	10.8	23.5	-	-	-	100.0

Table 2: Summary of run conditions and products

Run#	P (kb), T (˚C)	buffer	log fO_2	dopant	capsule	Starting § composition	Metal ¥	dura-tion	Ol-liq †	pha
158A	0.001, 1300	HM	-1.65	Ru, Cr, Ni (1 wt%)	AuPd	ank	none	52	-	gl,
158B	"	"	"	Rh, Os, Cr (1 wt%)	AuPd	ank	RhOsAuPd	"	-	gl,
160A	0.001, 1300	MHO	-3.03	Ru, Cr, Ni (1 wt%)	AuPd	ank	Ru	48	-	gl,
160B	"	"	"	Rh, Os, Cr (1 wt%)	AuPd	ank	RhOsAuPd	"	-	gl,
206A	0.001, 1264	MHO	-3.39	Re, Ni, Cr (1 wt%)	AuPd	ank	RhOsAuPd	42	93/92	gl, sp
206B	"	"	"	Rh, Os, Cr (1 wt%)	Pt	ank	RhOs	"	91/91	gl, sp
162A	0.001, 1300	RRO	-5.07	Ru, Cr, Ni (1 wt%)	AuPd	ank	RuReAuPd	48	-	gl,
162B	"	"	"	Rh, Os, Cr (1 wt%)	AuPd	ank	RhOsAuPd	"	-	gl,
159A	0.001, 1300	NNO	-6.49	Ru, Cr, Ni (1 wt%)	AuPd	ank	Ru	49	-	gl,
159B	"	"	"	Rh, Os, Cr (1 wt%)	AuPd	ank	RhOsAuPd	"	-	gl,
165A	0.001, 1300	HM	-1.65	Re, Ni, Cr (1 wt%)	AuPd	ank	none	50	96/94	gl, sp
165B	"	"	"	Ir, Ni, Cr (1 wt%)	AuPd	ank	IrPdAu	"	-	gl,
167A	0.001, 1300	MHO	-3.03	Re, Ni, Cr (1 wt%)	AuPd	ank	none	48	-	gl,
167B	"	"	"	Ir, Ni, Cr (1 wt%)	AuPd	ank	IrPdAu	"	-	gl, sp
166A	0.001, 1300	RRO	-5.07	Re, Ni, Cr (1 wt%)	AuPd	ank	none	52	-	gl,
166B	"	"	"	Ir, Ni, Cr (1 wt%)	AuPd	ank	none	"	-	gl,
164A	0.001, 1300	NNO	-6.49	Re, Ni, Cr (1 wt%)	AuPd	ank	none	48	92/90	gl, sp
164B	"	"	"	Ir, Ni, Cr (1 wt%)	AuPd	ank	IrPdAu	"	97/94	gl, sp
153A	0.001, 1300	NNO	-6.49	Pt, Re	Pt	DiAn	Re,Pt	36	-	gl,
112	19, 1275	None (Ru)	<-1.5	Pt, Re	Pt	Euc	Ru	24	-	gl, sp cp
118	20, 1275	Ru-RuO_2	-1.5	Pt, Re, Ru	Pt	euc	Ru	50	-	gl,

† olivine compositions predicted / measured; measured values reported in Table 5, and predicted values use the method of Snyder and Carmichael (1992).

¥ some metals were analyzed quantitatively (Table 6); the results listed in this table are based on energy dispersive spectra obtained for each run product.

§ Ank = ankaramite, DiAn = diopside-anorthite euctectic composition, euc = synthetic eucrite

Table 3: Electron microprobe analyses of spinels (average of n analyses).

run	n	SiO_2	TiO_2	Al_2O_3	Cr_2O_3	FeO_t	MnO	MgO	NiO	RuO_2	FeO§	Fe_2O_3§	Total
158A	10	-	1.67	9.47	8.46	49.80	-	14.94	6.73	-	1.64	53.52	96.43
B	20	-	1.14	9.84	22.34	38.10	-	17.66	0.43	-	3.10	38.90	93.41
160A	10	-	1.50	12.28	25.47	37.22	-	13.67	4.37	-	8.95	31.41	97.66
B	8	-	2.28	13.06	20.41	41.67	-	15.08	0.65	-	10.85	34.25	96.58
206A	10	-	0.96	21.12	27.26	29.91	-	18.31	0.17	-	7.76	24.61	100.19
B	8	-	1.98	10.97	17.53	46.31	-	10.52	8.44	-	10.57	39.71	99.72
162A	6	-	2.71	29.44	23.74	22.49	-	15.50	0.73	-	9.92	13.97	96.01
B	11	-	1.94	13.59	27.98	34.83	-	13.15	1.02	-	10.53	27.01	95.22
159A	7	-	2.29	24.76	31.97	17.48	-	18.79	1.78	-	4.06	14.91	98.56
B	8	-	2.17	16.22	47.33	11.77	-	18.28	1.95	-	3.48	9.21	98.64
165A	8	-	2.32	11.26	11.39	46.29	-	11.91	8.40	-	7.54	43.07	95.89
B	10	-	2.54	11.71	6.90	48.93	-	10.58	10.49	-	7.76	45.75	95.74
167A	10	-	2.49	13.02	10.76	49.01	0.28	12.17	5.33	-	10.76	42.51	97.32
B	10	-	2.25	10.90	7.55	54.60	0.33	13.10	5.43	-	9.12	50.54	99.22
166A	15	-	1.39	10.44	6.27	53.55	0.26	13.14	7.68	-	5.68	53.20	98.06
B	13	-	1.47	10.32	5.29	53.76	0.24	13.51	7.78	-	4.99	54.20	97.80
164A	10	-	1.47	25.78	33.65	18.77	-	16.79	1.10	-	10.15	9.58	98.52
B	5	-	5.80	24.66	20.20	22.84	-	21.88	0.89	-	6.16	18.54	98.13
112	9	0.50	0.05	29.17	0.53	39.40	0.06	5.49	18.45	-	9.47	33.26	96.98
118	10	0.21	0.02	11.11	0.28	63.30	0.12	5.23	11.38	3.98	16.02	52.54	100.80

§ FeO and Fe_2O_3 are calculated according to charge balance and stoichiometry after Carmichael (1967), and included in the analytical totals.

standard deviations of the mean for all elements are typically 2% or less.

Table 4: Electron microprobe analyses of glasses (average of n analyses).

run	n	SiO_2	TiO_2	Al_2O_3	Cr_2O_3	FeO*	MnO	MgO	CaO	Na_2O	K_2O	P_2O_5	NiO	ReO_2	Tota
158A	20	45.51	2.86	11.25	0.03	8.82	-	12.10	11.16	2.46	0.85	0.36	0.45	-	95.8
B	10	47.83	3.17	12.45	0.02	8.96	-	11.49	12.29	0.42	0.06	0.39	0.11	-	97.2
160A	10	47.03	3.06	12.50	-	9.96	-	12.32	11.77	0.30	0.04	0.38	0.44	-	97.8
B	9	45.54	2.96	12.11	0.03	9.61	-	12.52	11.65	0.30	0.03	0.39	0.34	-	95.5
206A	10	45.89	3.03	12.03	0.06	10.38	0.17	11.60	11.34	1.79	0.88	0.39	0.06	-	97.6
B	8	44.59	2.97	11.95	0.03	12.72	0.22	11.44	11.04	0.44	0.08	0.42	0.86	-	96.7
162A	10	49.62	3.57	13.15	0.12	12.51	-	13.19	3.69	0.22	0.03	0.40	0.11	-	96.6
B	9	45.37	2.88	11.96	0.18	11.60	-	11.52	10.95	1.37	0.50	0.40	0.11	-	96.8
159A	10	49.20	3.34	13.59	0.13	5.20	-	13.15	12.24	1.73	0.59	0.42	0.18	-	99.7
B	7	52.21	3.36	13.69	0.08	1.76	-	12.10	13.01	0.56	0.08	0.49	0.03	-	97.3
165A	10	45.28	2.92	11.43	0.04	10.20	0.17	11.73	11.33	2.03	0.19	0.33	0.59	0.17	96.4
B	10	44.96	2.88	11.64	0.05	11.12	0.21	12.22	11.21	0.94	0.04	0.36	0.76	-	96.3
167A	15	44.80	2.99	11.96	0.05	13.06	0.22	12.59	10.47	0.99	0.04	0.36	0.52	-	98.0
B	14	49.59	3.24	13.47	0.02	7.20	1.37	11.97	10.39	0.48	0.07	0.43	0.28	-	98.5
166A	13	45.91	3.01	12.05	0.04	12.00	0.22	12.75	10.34	0.23	0.01	0.36	0.59	0.08	97.5
B	12	45.99	2.84	11.61	0.03	11.99	0.20	14.07	9.81	0.04	0.01	0.34	0.67	-	97.5
164A	10	47.09	3.39	13.61	0.13	5.96	0.18	11.48	12.72	2.56	0.59	0.40	0.27	0.21	98.6
B	10	58.04	2.83	11.53	0.19	2.06	0.16	13.46	9.37	0.87	0.20	0.28	0.03	-	99.0
153A	29	49.94	-	12.07	-	-	-	11.00	23.88	-	-	-	-	-	96.9
112	10	53.28	0.07	16.34	0.01	9.46	0.10	4.90	10.90	0.07	0.02	0.02	1.07	-	96.2
118	10	55.35	0.04	16.00	0.01	6.68	0.11	4.05	8.62	0.10	0.02	0.02	0.34	2.52	93.8

standard deviations of the mean for all elements are typically 2% or less.

Table 5: Electron microprobe analyses of silicates (average of n analyses)

run	phase	n	SiO_2	TiO_2	Al_2O_3	Cr_2O_3	FeO*	MnO	MgO	CaO	NiO	Total
206A	olivine	10	40.62	0.01	0.11	0.04	8.15	0.22	50.41	0.29	0.12	99.97
206B	olivine	12	38.73	0.04	0.10	0.03	7.74	0.19	45.01	0.27	7.55	99.66
165A	olivine	8	40.36	0.03	0.11	0.06	5.40	0.16	48.19	0.26	3.24	97.81
164A	olivine	8	40.26	0.03	0.10	0.11	9.30	0.16	47.84	0.31	1.29	99.40
164B	olivine	8	41.45	0.03	0.07	0.13	6.11	0.15	51.54	0.27	0.39	100.11
153A	clinopyroxene	17	55.04	-	0.76	-	0.04	-	18.79	25.53	-	100.16
112	orthopyroxene	10	48.72	0.01	7.00	0.03	12.76	0.12	20.26	1.47	7.92	98.29
112	clinopyroxene	7	46.60	0.03	9.16	0.04	9.84	0.10	11.10	17.33	4.03	98.28

standard deviations of the mean for all elements are typically 2% or less.

Table 6: Electron microprobe analyses of metals (average of n analyses)

run	n	Fe	Ni	Ru	Rh	Os	Re	Au	Pd	Total
162B	1	-	-	57.27(50)	-	-	26.05(40)	9.24(25)	6.01(31)	98.57
159A	3	0.28(2)	0.12(1)	96.95(90)	0.97(7)	0.04(2)	-	-	-	98.36
B	3	0.71(3)	0.27(4)	-	56.77(50)	41.46(20)	-	-	-	99.21
112	2	-	-	100.4(1.0)	-	-	-	-	-	100.4
118	1	-	-	99.72(90)	-	-	0.14(8)	-	-	99.86

standard deviations of the mean for all elements are typically 2% or less.

Table 7: Summary of SIMS data and partition coefficients

run	$^{101}Ru/^{30}Si$ glass	Ru in glass ppm	Ru in chromite (EMPA - ppm)	D(Ru)
158A	5.30×10^{-4}	217(20)	21600(1000)	100(10)
160A	2.89×10^{-6}	1.18(12)	-	-
"	2.56×10^{-6}			
162A	1.93×10^{-6}	1.05(10)	1200(60)	1143(115)
159A	2.02×10^{-6}	0.83(8)	-	-

run	$^{103}Rh/^{30}Si$ glass	Rh in glass ppm	Rh in chromite (EMPA - ppm)	D(Rh)
158B	8.10×10^{-5}	8.5(9)	4500(450)	530(105)
	9.44×10^{-5}	9.9(9)	"	450(90)
	1.16×10^{-4}	12(1)	"	370(75)
160B	9.05×10^{-5}	9.5(9)	390(40)	41(8)
	8.71×10^{-5}	9.2(9)	"	42(8)
162B	8.68×10^{-5}	9.1(9)	490(50)	54(11)
	8.25×10^{-5}	8.7(9)	"	56(11)
159B	5.54×10^{-5}	5.8(6)	410(40)	71(14)
	4.25×10^{-5}	4.5(5)	"	91(18)

numbers in parentheses represent the standard deviation from the mean of the analyses (see text).

Table 8: Summary of LA-ICP-MS data and partition coefficients (ppm)

run	Ru in glass	Ru in spinel	Ru in olivine	D(Ru) spinel/gl	D(Ru) oliv/gl
158A	120(4)	9130(337)	28(1)	76(6)	0.23(2)
118	85(5)	74000(3700)	-	871(90)	-
	97(5)	84000(4200)	-	866(90)	-

	Pd in glass	Pd in spinel	Pd in olivine	D(Pd) spinel/gl	D(Pd) oliv/gl
158A	82(3)	11.7(9)	9.8(5)	0.14(2)	0.12(1)

	Au in glass	Au in spinel	Au in olivine	D(Au) spinel/gl	D(Au) oliv/gl
158A	16.7(6)	1.3(3)	2.1(1)	0.076(10)	0.12(2)

run	Re in glass	Re in spinel	Re in olivine	D(Re) spinel/gl	D(Re) oliv/gl
164A	1110(56)	69(4)	41(2)	0.062(12)	0.017(6)
	1080(55)	-	17(1)	-	-
	1050(54)	-	-	-	-
165A	1034(53)	104(6)	75(4)	0.10(1)	0.073(7)
166A	132(7)	2.9(3)	-	0.025(3)	-
167A	400(20)	3.5(4)	-	0.0087(13)	-
118	23800(1200)	150(8)	-	0.006(1)	-
	35000 (1800)	470(24)	-	0.013(1)	-

run	Re in glass	Re in cpx	Pt in glass	Pt in cpx	D(Re) cpx/gl	D(Pt) cpx/gl
153A	2.19(10)	0.40(6)	5.79(57)	8.68(1.05)	0.18(4)	1.50(36)

run	Re in glass	Re in olivine	Re in opx	Re in cpx	Re in spinel	D(Re) oliv/gl	D(Re) opx/gl	D(Re) cpx/gl	D(Re) spinel/gl
112	156(8)	-	2.0(1)	33(2)	33(2)	-	0.013(1)	0.21(1)	0.21(1)
206	571(21)	14.8(6)	-	-	0.70(2)	0.026(2)	-	-	0.0012(1)

run	Ir in glass	Ir in spinel	D(Ir) spinel/gl
165B	0.028(4)		
"	0.034(4)		
"	0.038(4)		
166B	10.7(5)	444(18)	5-132
"	19.5(8)	106(4)	
"	3.7(2)	259(10)	
167B	0.037(8)	50(2)	230 -
	0.197(13)	4320(173)	22000
	0.024(4)	190(8)	
		4370(175)	

numbers in parentheses represent one sigma error for each element, and include both counting statistics and instrumental reproducibility (see text).

Table 9. Upper limits of oxide and argide interference rates determined by LA-ICP-MS analysis of NIST SRM 611 and SRM 1158.

Isotope	Interfering molecule	SRM	MO^+/M^+ or MAr^+/M^+
^{101}Ru	$^{61}Ni^{40}Ar$	1158	$7.5x10^{-5}$
^{101}Ru	$^{85}Rb^{16}O$	611	$4.9x10^{-6}$
^{105}Pd	$^{65}Cu^{40}Ar$	1158	$8.9x10^{-5}$
^{105}Pd	$^{89}Y^{16}O$	611	$2.0x10^{-4}$
^{188}Os	$^{148}(SmNd)^{40}Ar$	611	$1.6x10^{-5}$
^{188}Os	$^{172}Yb^{16}O$	611	$1.8x10^{-5}$
^{189}Os	$^{149}Sm^{40}Ar$	611	$1.4x10^{-5}$
^{189}Os	$^{173}Yb^{16}O$	611	$1.7x10^{-5}$
^{190}Os	$^{150}(SmNd)^{40}Ar$	611	$2.2x10^{-5}$
^{190}Os	$^{174}Yb^{16}O$	611	$8.0x10^{-6}$
^{191}Ir	$^{151}Eu^{40}Ar$	611	$8.2x10^{-5}$
^{191}Ir	$^{175}Lu^{16}O$	611	$4.3x10^{-5}$
^{192}Os	$^{152}Sm^{40}Ar$	611	$8.3x10^{-5}$
^{192}Os	$^{176}(YbHfLu)^{16}O$	611	$1.0x10^{-4}$
^{193}Ir	$^{153}Eu^{40}Ar$	611	$5.3x10^{-5}$
^{193}Ir	$^{177}Hf^{16}O$	611	$1.7x10^{-4}$

Figure Captions

Figure 1: T-fO_2 range of experiments from this study. Buffers shown are the Ru-RuO_2 (O'Neill and Nell, 1997), hematite-magnetite (HM; Myers and Eugster, 1983), MnO-Mn_3O_4 (MHO; O'Neill and Pownceby, 1993b), Re-ReO_2 (RRO; Pownceby and O'Neill, 1994), Ni-NiO (NNO; O'Neill and Pownceby, 1993a) and Fe-FeO (IW; O'Neill and Pownceby, 1993a). The shaded region is the T-fO_2 zone of terrestrial magmas taken from Carmichael (1991).

Figure 2A: Back scattered electron (BSE) image of run product from run 158A (1300 ˚C, 1 bar, and hematite-magnetite buffer; Table 2) showing large spinels, larger glassy regions and Ru metal; **2B:** BSE image of run product from run 112 (1275 ˚C, 19 kbar, and near the hematite-magnetite buffer; Table 2) showing spinel, glass and Ru metal. Scale bars in both images are 50 microns.

Figure 3: Rh (ppm) vs. $^{101}Rh^{+}/^{30}Si^{+}*SiO_2$ for experimental glasses used by Capobianco et al. (1994) and in this study for SIMS calibration for Rh analysis.

Figure 4A: The plot of D(Re) spinel/melt vs. logfO_2 shows Re is incompatible in Cr-bearing spinels, and D(Re) spinel/melt is not obviously dependent upon oxygen fugacity. **Figure 4B:** D(Re) spinel/melt may be a function of the Re content of the spinel, as has been observed for other elements in spinels (Ni, Co, V; Righter, 2002), but this does not hold true for the entire dataset and thus awaits further investigation.

Figure 5A,B: D(Rh) for spinel/melt indicating that Rh remains as compatible in Cr-bearing spinels as it is in high hercynite- and magnetite-component spinels (Capobianco and Drake, 1990; Capobianco et al., 1994). Inverse spinels generally have higher partition coefficients for Rh (A), but spinels with higher concentrations of Rh may also have higher partition coefficients (B). Numbers next to symbols are logfO_2 values from Table 2, and show that there is no systematic

behavior with variable fO_2.

Figure 6A: Dependence of D(Ru) spinel/melt on oxygen fugacity. New experiments using Cr-bearing spinels, together with previous work on aluminous and magnetite-rich spinels (Capobianco and Drake, 1990; Capobianco et al., 1994) indicate increasing D(Ru) at lower oxygen fugacities. This may reflect a change in valence from 4+ to 3+ at lower oxygen fugacities, but constraints on the specific valence of Ru remain poor. **Figure 6B:** Within the Capobianco and Drake (1990) and Capobianco et al. (1994) data sets there are trends of increasing D(Ru) with increasing Ru concentration in the spinel. However, our new data do not support such a dependence upon Ru concentration in the spinel.

Figure 7A and B: Cr, Ru and Pd vs. MgO in the Kostomuksha komatiite suite (from Puchtel and Humayun, 2000). Major element modelling of crystal fractionation of the proposed Kostomuksha parent liquid (Puchtel and Humayun, 2000; Puchtel et al., 1998) was carried out using the MELTS program (Ghiorso and Sack, 1994) from 1700 to 1200 ˚C, at 2 kb and the QFM oxygen buffer. Asterisks indicate the calculated trends using the major element results (at 25 ˚C intervals), and the following partition coefficients: D(Ru) olivine/melt = 1 (based on this study and that of Brenan et al., 2002, 2003 at low fO_2), D(Ru) spinel/melt = 1000, D(Pd) olivine/melt = 0.1, D(Pd) spinel/melt = 0.1 (based on this study). D(Cr) olivine/melt = 0.36, D(Cr) spinel/melt = 200, were chosen based on the compilation of Green (1994) and Roeder and Reynolds (1991). The amount of olivine fractionated before chromite saturation is 20.5%, and the amount after is 32.9 %.

Figure 8: Cr vs. Ru and Ir for the Vetreny Belt komatiitic basalt suite (from Puchtel and Humayun, 2001). Major element modelling of crystal fractionation was carried out using the MELTS

program (Ghiorso and Sack, 1994) from 1400 to 1100 ˚C, at 1 bar and the QFM oxygen buffer. Dashed lines indicate the calculated trends using the major element results (tips of arrowed lines represent fractionation of 17.4% olivine and 0.38% spinel) and the following partition coefficients: D(Ru) olivine/melt = 1, D(Ru) spinel/melt = 1000 (chosen based on this study and that of Brenan et al., 2002 at low fO_2), D(Ir) olivine/melt = 1 (based on work of Brügmann et al., 1987), D(Ir) spinel/melt = 250 to 2000 (this study), D(Cr) olivine/melt = 0.36 (from compilation of Green, 1994), and D(Cr) spinel/melt = 250 (from Roeder and Reynolds, 1991). "Olivine only" lines represent trends expected using the olivine/melt partition coefficients determined here, fractionation of 17.4% olivine, but assuming incompatibility of Ru and Ir in spinel; these show that chromite is required to produce the observed trends. Series of dashed lines for Ir indicate the effect of raising D(Ir) spinel/melt from 250 to 2000.

Figure 9: Plot of MgO vs. Cr, Pt, Pd, Rh, and Ir in the Cape Smith Fold Belt basaltic komatiite suite (from Barnes and Picard, 1993). Major element modelling of crystal fractionation was carried out using the MELTS program (Ghiorso and Sack, 1994); MgO, Cr and Ni trends are reproduced with 28% olivine and 1.5% chromite fractionation throughout the sequence. Lines indicate calculated trends using the MELTS results, and the following partition coefficients: D(Ir) olivine/melt = 1 (based on work of Brügmann et al., 1987), D(Ir) spinel/melt = 200 to 600 (this study), D(Rh) olivine/melt = 1 (based on Capobianco et al., 1991), D(Rh) spinel/melt = 75 (this study), D(Pd) olivine/melt = 0.1 (this study), D(Pd) spinel/melt = 0.1 (this study), D(Pt) olivine/melt = 0.1, D(Pt) spinel/melt = 0.1 (from Puchtel and Humayun, 2000; Righter et al., 2000), D(Cr) olivine/melt = 0.3 (from compilation of Green, 1994), D(Cr) spinel/melt = 250 (Roeder and Reynolds, 1991), D(Ni) spinel/melt = 15 (Righter, 2002), and D(Ni) olivine/melt = 10 (Green,

1994). Series of dashed lines for Ir show the effect of raising D(Ir) spinel/melt from 200 to 600.

Figure 10: Re (ppt) vs. Ni (ppm) for Hawaiian Drilling Project samples (circles; Hauri et al., 1996; Rhodes, 1996), and Volcan Alcedo, Galapagos Islands (triangles; Righter et al., 1998). Solid line indicates Re-Ni trend expected during fractionation of olivine and chromite in 75:1 ratio using D(Re) oliv/liquid = 0.01 (this study), D(Re) spinel/melt = 0.01 (this study), D(Ni) spinel/melt = 15 (Righter, 2002), and D(Ni) olivine/melt = 10 (Green, 1994). For the Galapagos suite, t he initial rise in Re concentration with decreasing Ni is due to olivine, augite and plagioclase fractionation, then Re concentration drops when magnetite and late sulfide join the fractionating mineral assemblage.

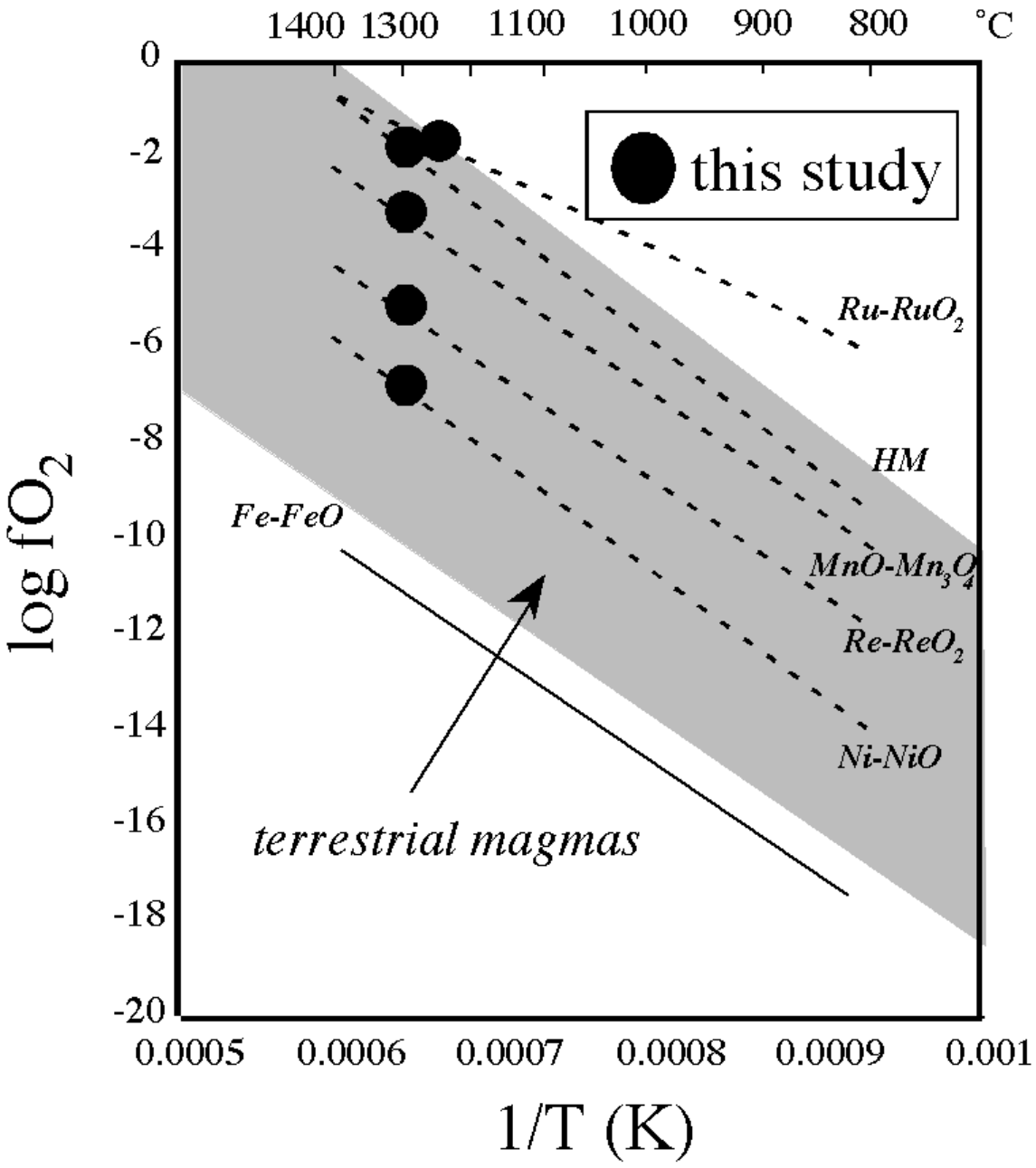
1400 1300 1100 1000 900 800 °C
0
-2
-4
-6
-8
-10
-12
-14
-16
-18
-20
log fO2
this study
Ru-RuO2
HM
Fe-FeO
MnO-Mn3O4
Re-ReO2
Ni-NiO
terrestrial magmas
0.0005 0.0006 0.0007 0.0008 0.0009 0.001
1/T (K)

Figure 1

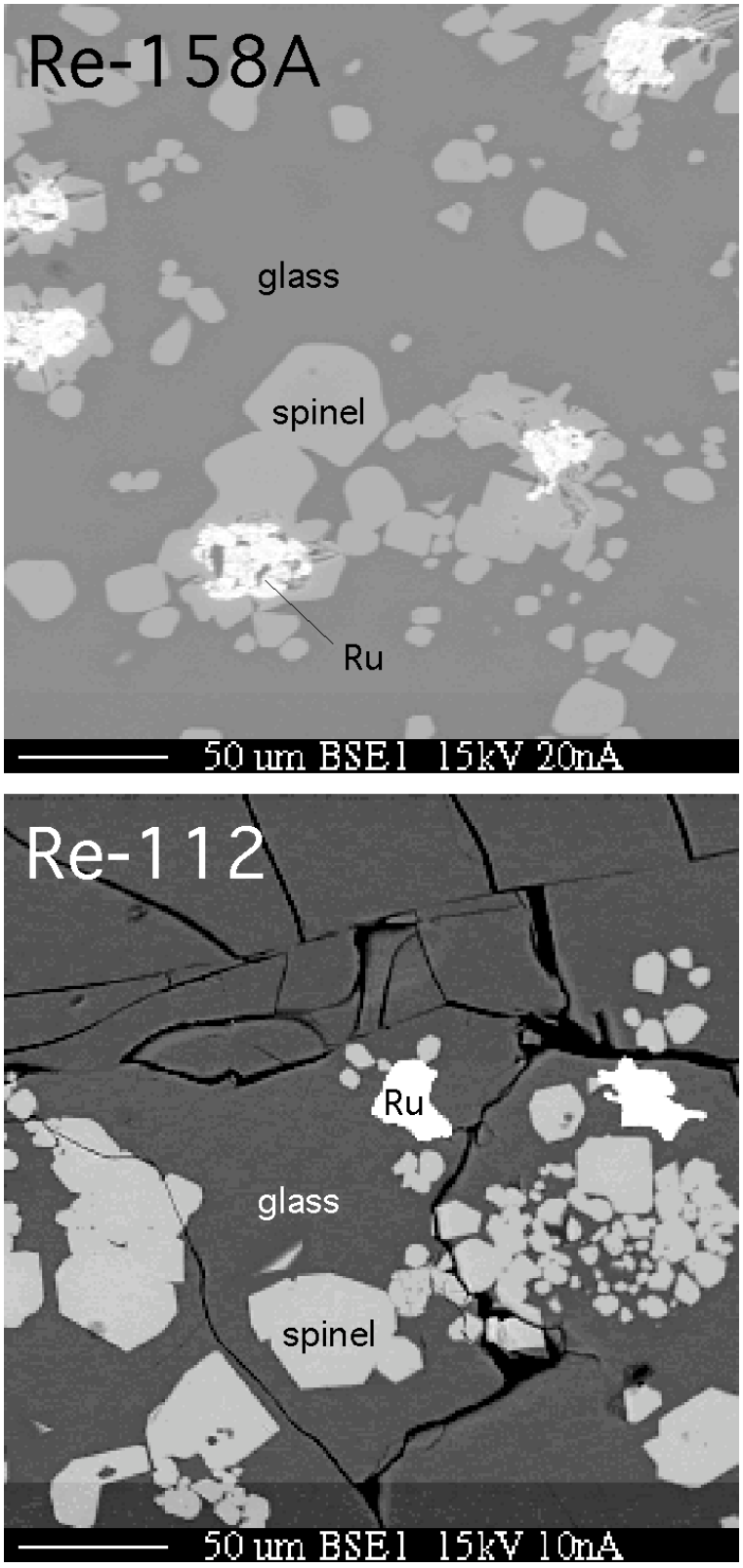
Re-158A
glass
spinel
Ru
50 um BSE1 15kV 20nA
Re-112
Ru
glass
spinel
50 um BSE1 15kV 10nA

Figure 2

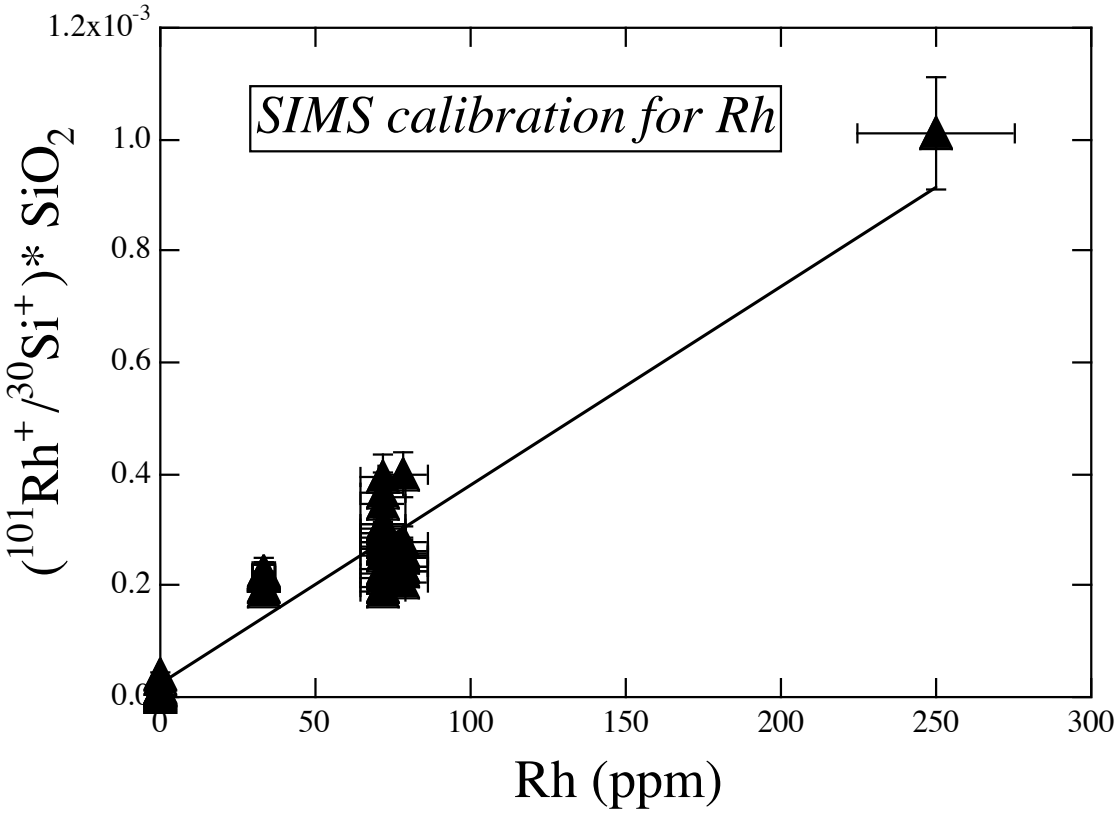
SIMS calibration for Rh
1.2x10-3
1.0
0.8
0.6
0.4
0.2
0.0
0
50
100
150
200
250
300
Rh (ppm)
(101Rh+ /30Si+)* SiO2

Figure 3

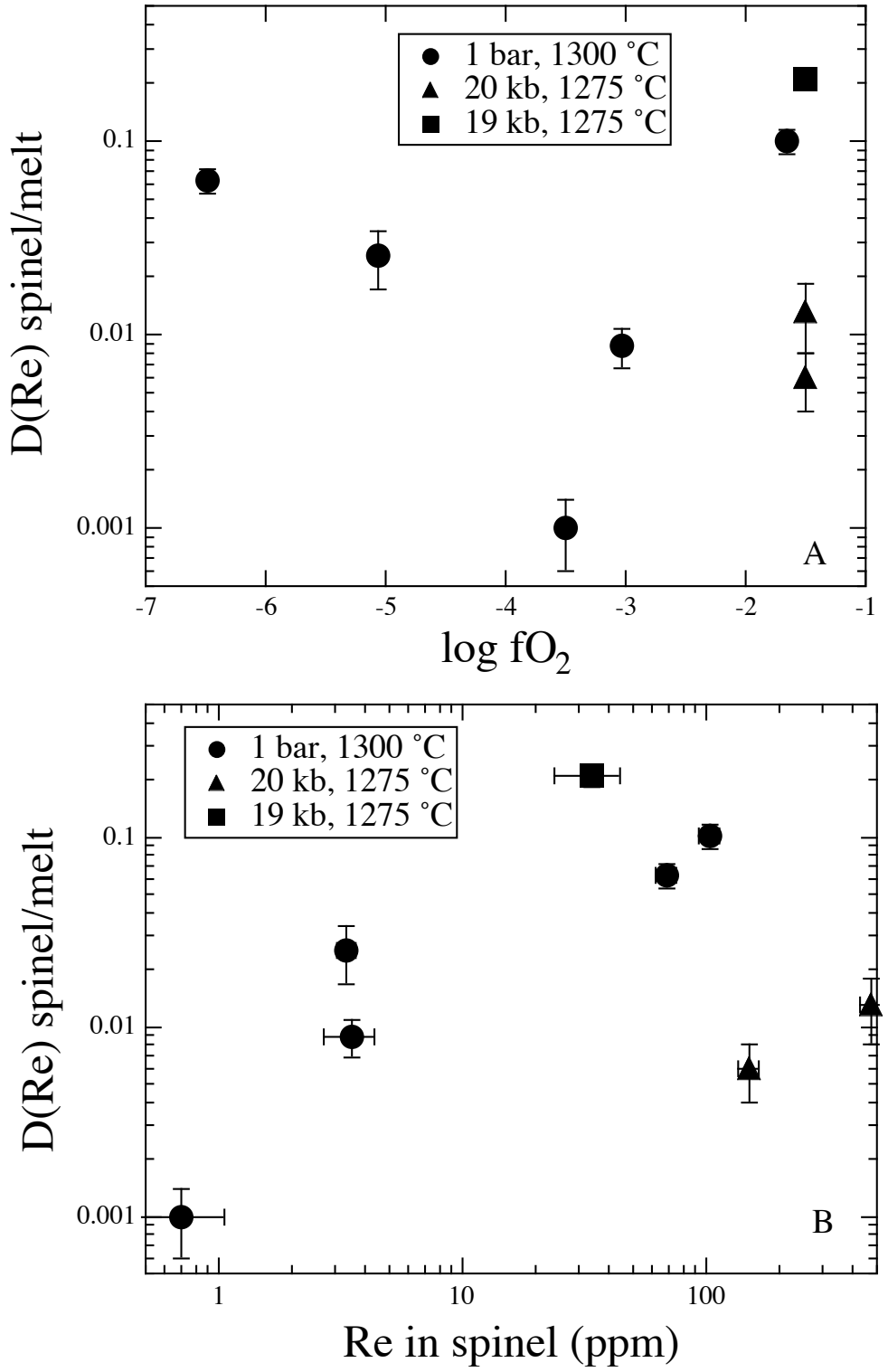
1 bar, 1300 ˚C
20 kb, 1275 ˚C
19 kb, 1275 ˚C
D(Re) spinel/melt
0.1
0.01
0.001
-7
-6
-5
-4
-3
-2
-1
log fO2
A
1 bar, 1300 ˚C
20 kb, 1275 ˚C
19 kb, 1275 ˚C
D(Re) spinel/melt
0.1
0.01
0.001
1
10
100
Re in spinel (ppm)
B

Figure 4

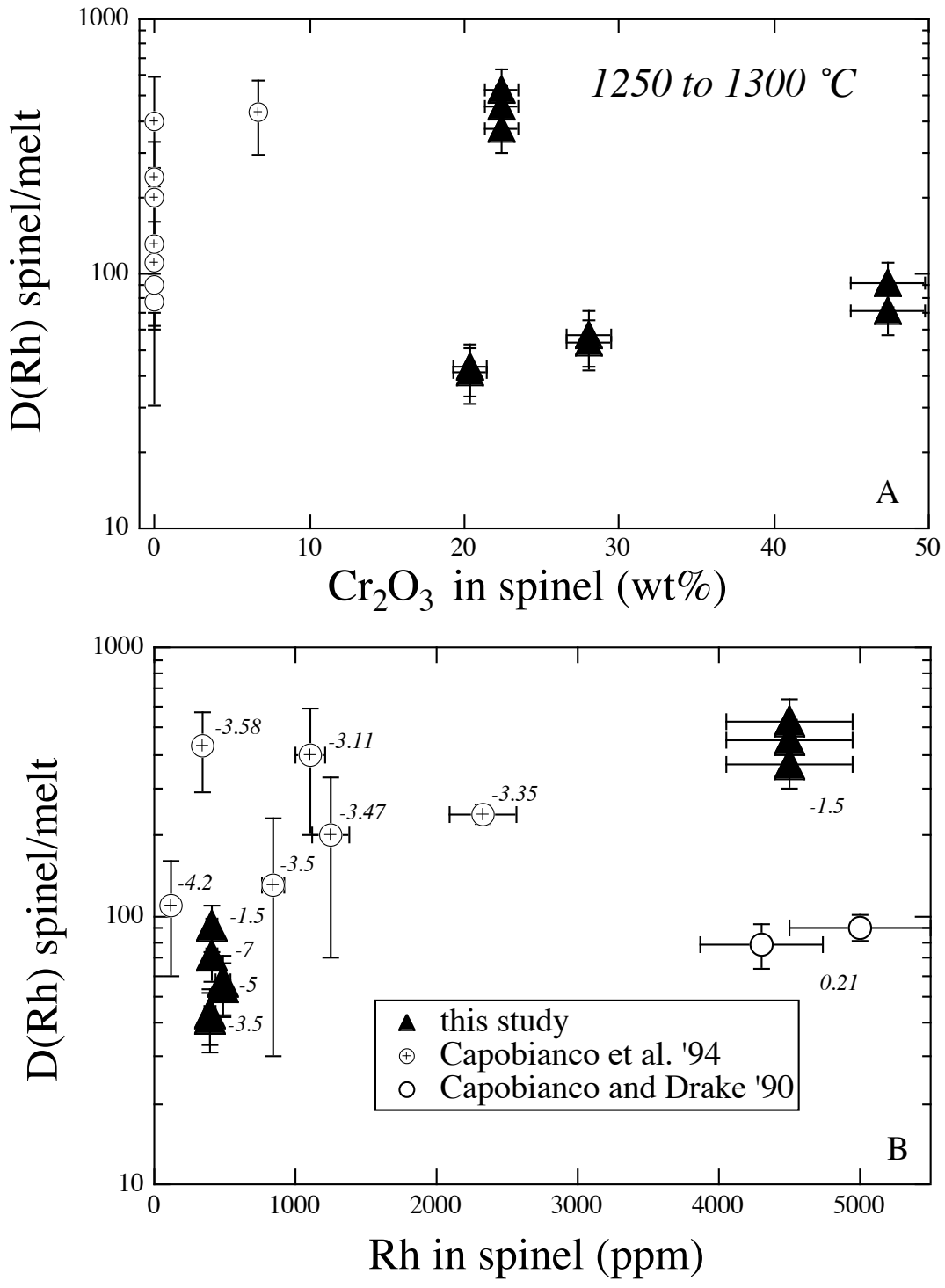
1250 to 1300 ℃
A
D(Rh) spinel/melt
Cr_2O_3 in spinel (wt%)
1000
100
10
0
10
20
30
40
50
B
-3.58
-3.11
-3.47
-3.35
-1.5
-4.2
-3.5
-1.5
-7
-5
-3.5
0.21
this study
Capobianco et al. '94
Capobianco and Drake '90
Rh in spinel (ppm)
1000
2000
3000
4000
5000

Figure 5

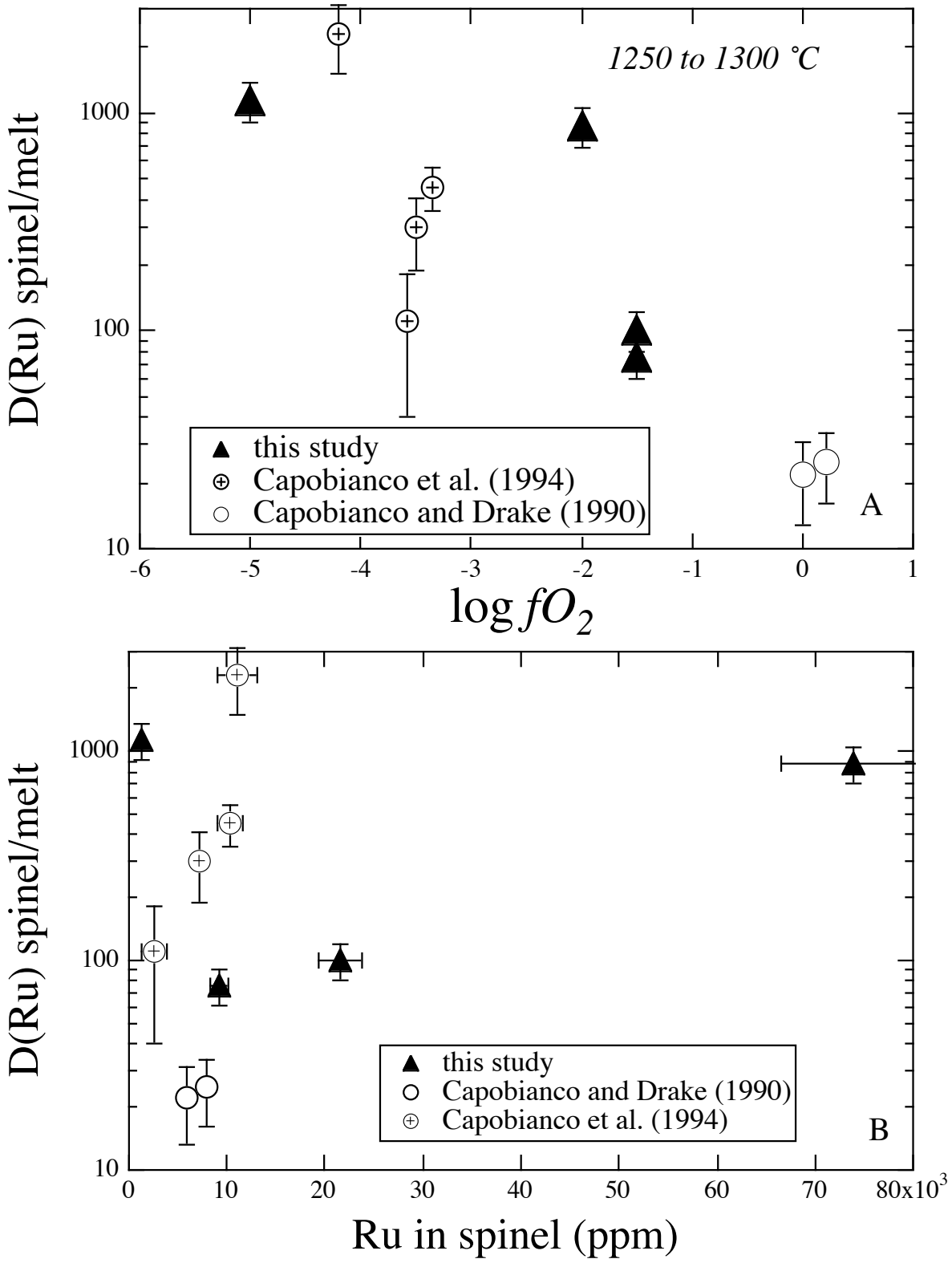
1250 to 1300 ˚C
D(Ru) spinel/melt
1000
100
10
-6
-5
-4
-3
-2
-1
0
1
log fO_2
this study
Capobianco et al. (1994)
Capobianco and Drake (1990)
A
D(Ru) spinel/melt
1000
100
10
0
10
20
30
40
50
60
70
80x10^3
Ru in spinel (ppm)
this study
Capobianco and Drake (1990)
Capobianco et al. (1994)
B

Figure 6

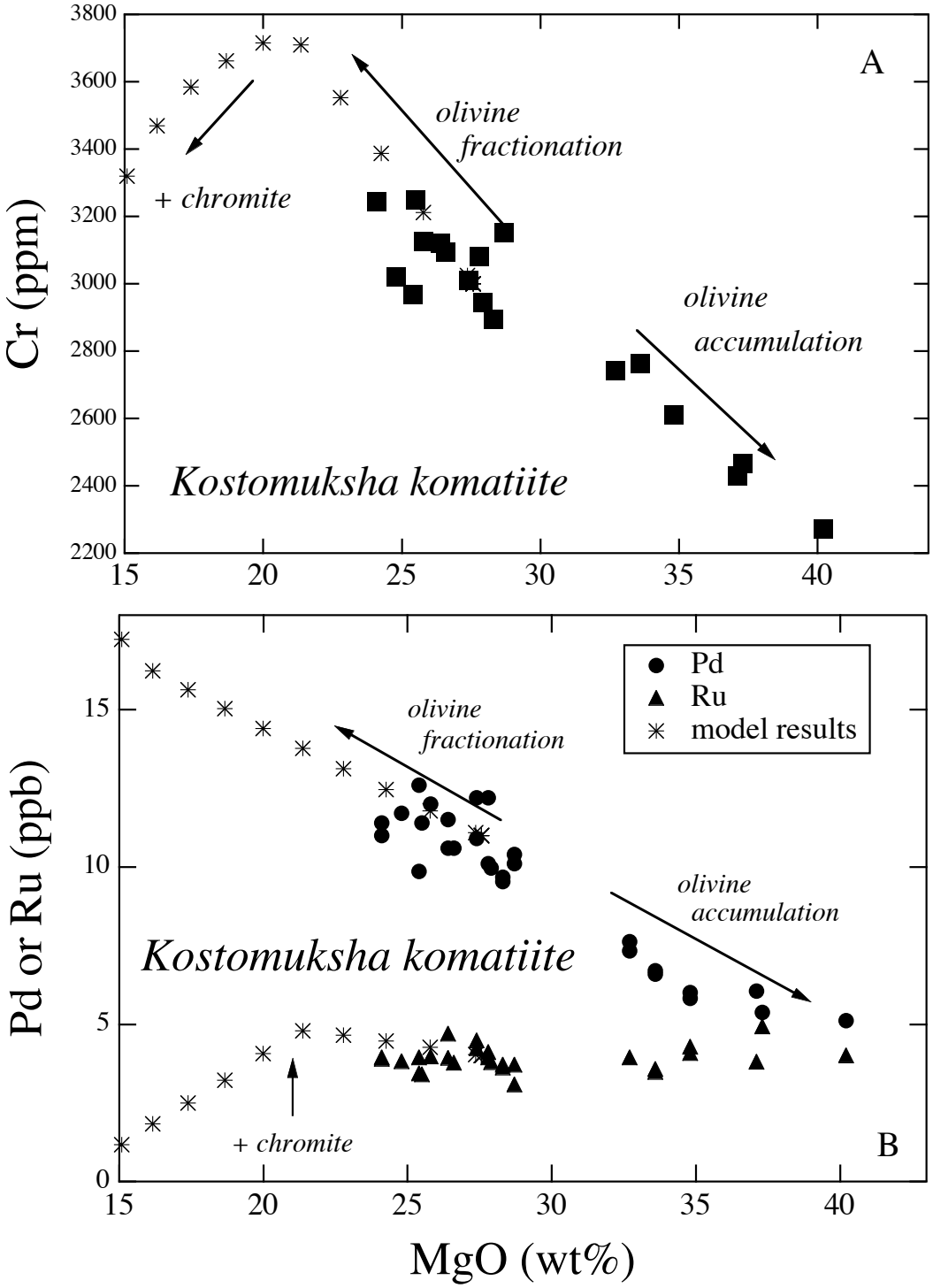
A
olivine
fractionation
+ chromite
olivine
accumulation
Kostomuksha komatiite
Cr (ppm)
3800
3600
3400
3200
3000
2800
2600
2400
2200
15
20
25
30
35
40
Pd
Ru
model results
olivine
fractionation
olivine
accumulation
Kostomuksha komatiite
+ chromite
B
Pd or Ru (ppb)
15
10
5
0
MgO (wt%)

Figure 7

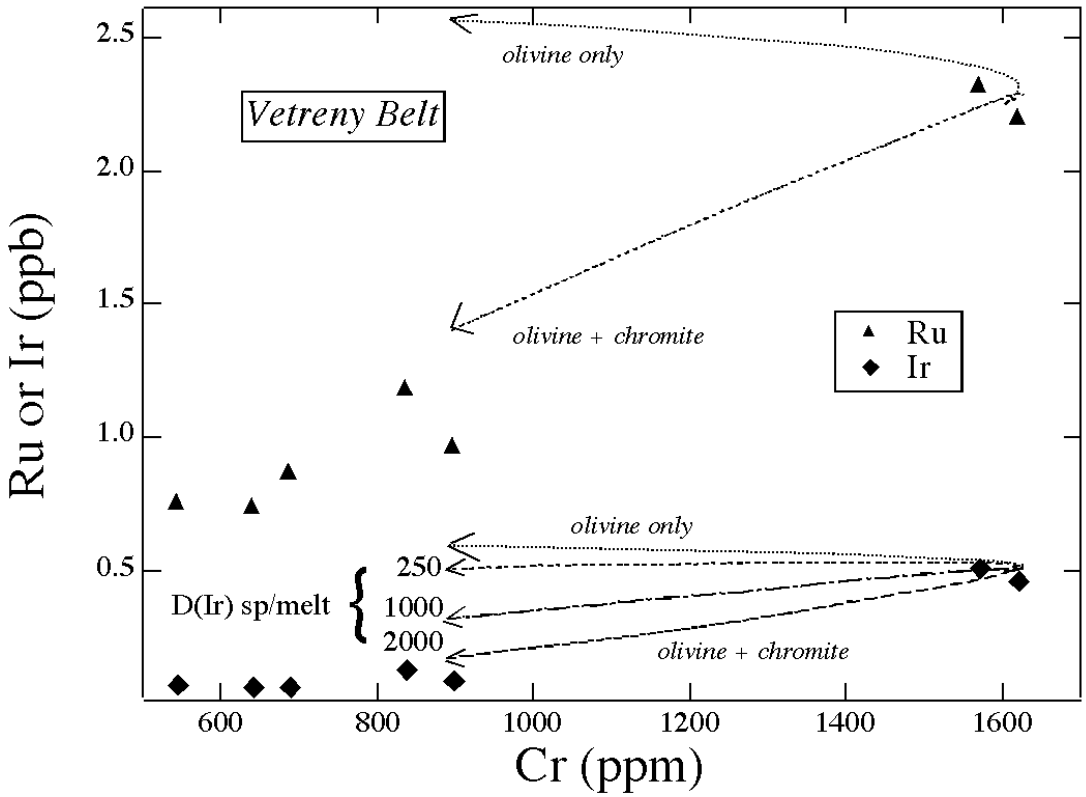
Vetreny Belt
olivine only
olivine + chromite
Ru
Ir
olivine only
D(Ir) sp/melt
250
1000
2000
olivine + chromite
Ru or Ir (ppb)
Cr (ppm)
2.5
2.0
1.5
1.0
0.5
600
800
1000
1200
1400
1600

Figure 8

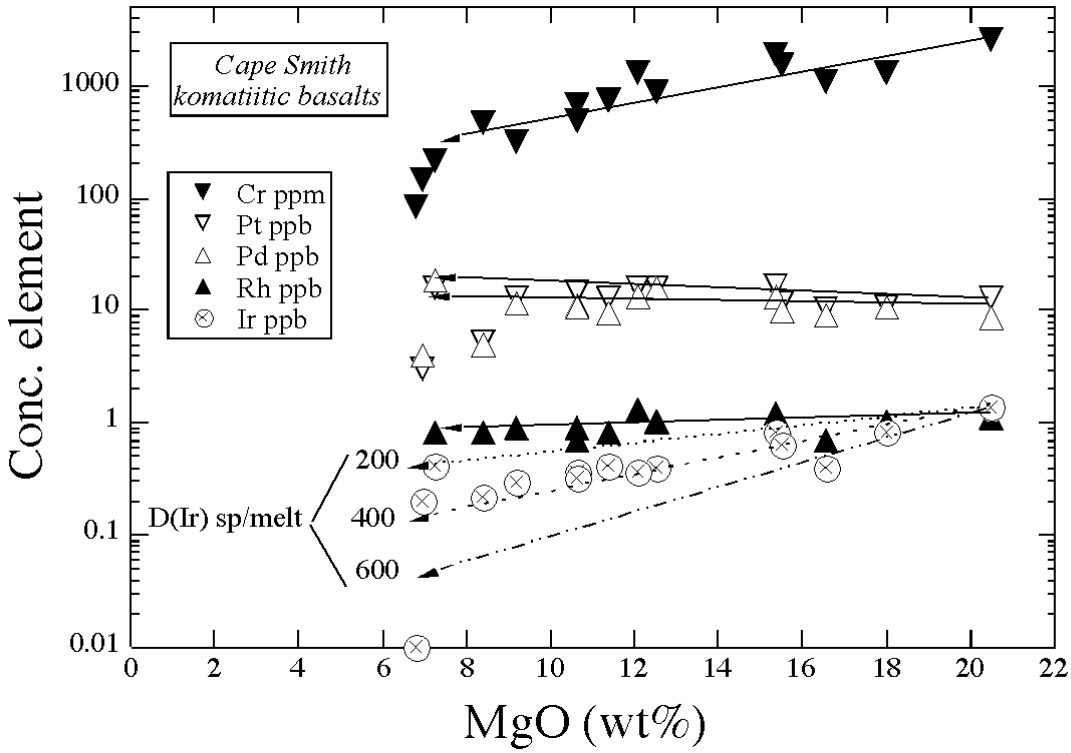
Cape Smith
komatiitic basalts
Cr ppm
Pt ppb
Pd ppb
Rh ppb
Ir ppb
D(Ir) sp/melt
200
400
600
Conc. element
MgO (wt%)
1000
100
10
1
0.1
0.01
0
2
4
6
8
10
12
14
16
18
20
22

Figure 9

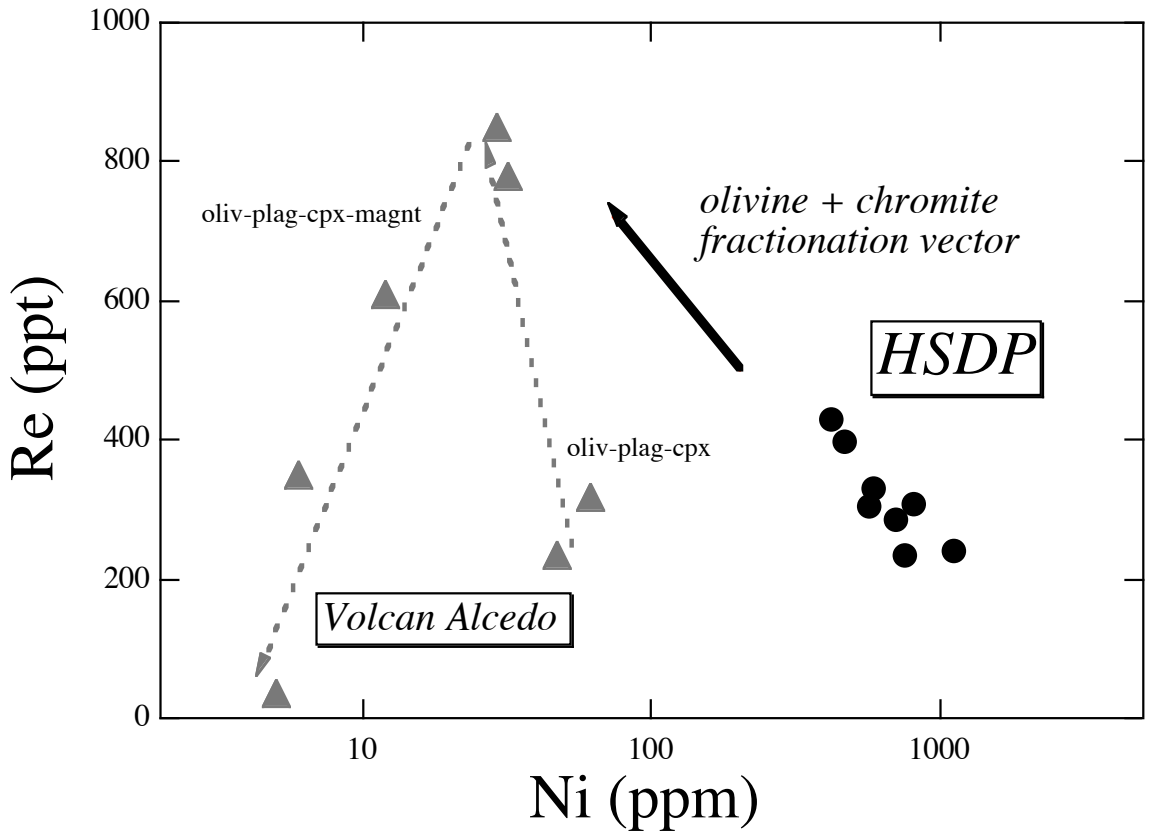
1000
800
600
400
200
0
Re (ppt)
10
100
1000
Ni (ppm)
oliv-plag-cpx-magnt
olivine + chromite
fractionation vector
HSDP
oliv-plag-cpx
Volcan Alcedo

Figure 10